# Dimpled frames: morphing attributes, multistability and feeble memory

Asifur Rahman, Paolo Celli*

*Department of Civil Engineering, Stony Brook University, Stony Brook, NY 11794, USA*

**Abstract**

The rise of mechanically intelligent systems – that sense, compute and adapt with minimal electronics – is increasing the need for devices that can store mechanical memory. Here, we introduce *dimpled frames* as structural analogs to soft multistable dimpled sheets, whose unique memory attributes manifest as a dependency of their final shape on the sequence of actuation of each bistable dimple. Our structures feature sinusoidal arches connected at multiple locations of a base with polygonal cutouts. Each arch can snap through a cutout, yielding local bistability and, potentially, global multistability. Through extensive experiments and efficient numerical simulations based on discrete elastic rods, we unveil the link between the geometrical parameters of our structures and their capacity to display mechanical memory. Specifically, we show that memory is "feeble" in our structures, and will vanish if the parameters are not chosen properly – shedding further light on the requirements for arrays of bistable units to display mechanical memory. Our dimpled frames – that can be made of stiff materials with low damping – could provide memory storage options for vibration-based mechanical computing systems.

*Keywords:* Morphing structures, Buckling, Multistability, Mechanical memory, Discrete elastic rods

## 1. Introduction

Shape-morphing structures are designed to respond to external stimuli by morphing between desired shapes [1, 2]. From toys such as Hoberman spheres to real engineering applications, morphing systems demonstrate how geometrical design and structural flexibility can yield adaptability and multi-functionality. Such systems can be widely applicable as morphing wings [3, 4] and deployable space structures [5, 6], soft robots capable of bioinspired locomotion [7, 8] and grasping [9, 10], biomedical devices that can be deployed inside the human body [11, 12], energy absorbers [13, 14], energy harvesters [15] and energy efficient building envelopes [16].

Here, we focus on bistable and multistable morphing structures, designed to snap between two or more stable states [17–21]. From a structural perspective, these systems are particularly attractive for their robustness and self-standing nature: they are capable of significant morphing, and yet they can remain in their stable states and bear loads [22–24] without the need for external inputs [25] or special boundary conditions [26]. Multistable structures are also gaining increasing traction as cornerstones of mechanically intelligent systems [27, 28] – that can can sense, compute and adapt without the need for electronics, and that can find applications in robotics and automation [29]. There are many elements needed for a mechanical system to be intelligent, and one of them is memory. Multistable systems are particularly suitable to store information in a non-volatile fashion, since they feature bit-like units that can be in a 0 (unsnapped) or 1 (snapped) state. Some mechanical memory storage devices feature arrays of uncoupled bistable units in parallel, where multiple actuators are needed to write and read information [30, 31]. Others feature series of bistable units coupled with springs, where units can be actuated through specific impulsive [32, 33], vibrational [34], or static inputs [35, 36], where some of these systems can also perform logical operations and computations rather than just storing memory [37, 38].

*Corresponding author
*Email addresses:* asifur.rahman@stonybrook.edu (Asifur Rahman), paolo.celli@stonybrook.edu (Paolo Celli)

The systems that are of interest to us are arrays of coupled bistable units that feature *morphological memory*, i.e., that can achieve drastically-different shapes depending on the sequence in which their units are actuated.

The prototypical multistable system with morphological memory is the dimpled sheet – made of spherical bistable domes arranged following regular patterns on a thin plate. While early versions of these systems were made of metal and had an irreversible behavior [39], recent incarnations are soft, elastomeric, and behave elastically [40–42]. A single dimple is sketched in Fig. 1a; when pressing down on it, it can snap and invert its shape, inducing curvature changes in the surrounding plate, as shown in Fig. 1b. When planar arrays of such units are snapped, they can generate complex three dimensional (3D) stable shapes [41]; snapping the units in different sequences leads to distinct shapes. Why? In essence, these systems are multistable when all units are snapped, and the strong coupling between units (through the base sheet) biases the shape of the array towards one of those available stable shapes. In these sheets, the capability of achieving complex 3D shapes is lost as the spacing between units is increased [42]. While these sheets show amazing morphing capacity and memory storage potential, being made of soft materials limits their applicability. In fact, many mechanical computing devices rely on vibrations and elastic wave manipulation to perform logic and computing operations [28, 43–46], and will likely need memory storage units that are made of materials that can propagate vibration and elastic wave signals – something that soft elastomers cannot do very well.

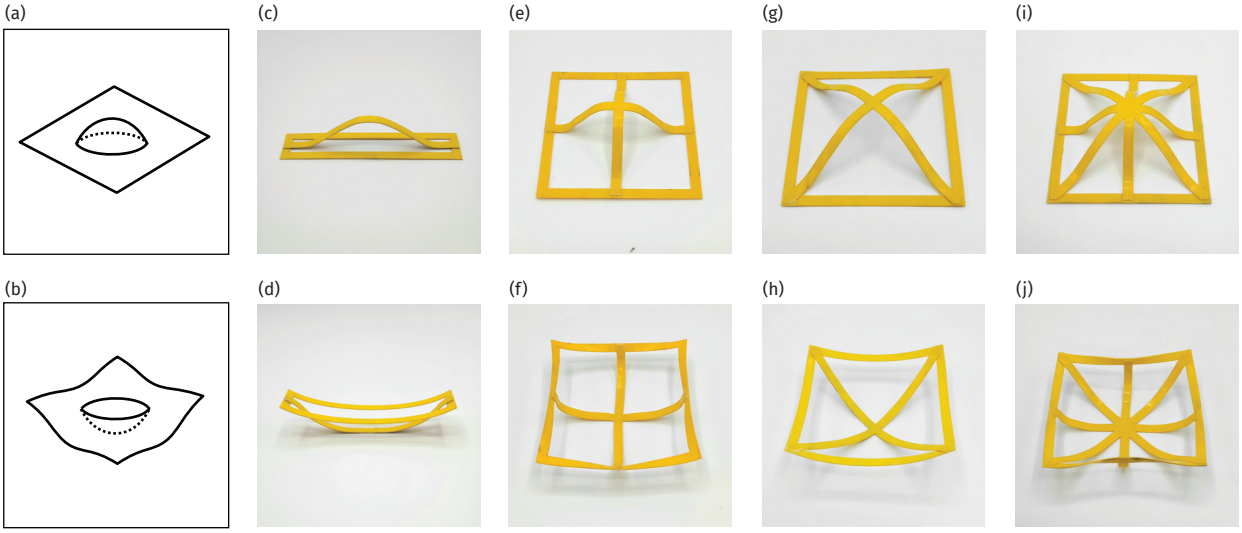


Fig. 1: The genesis of our dimpled frames. A soft bistable dimple unit, serving as inspiration for our work, is schematically shown in its (a) first (undeformed) and (b) second (deformed) stable states. (c) 1D unit from our previous work [47], featuring a sinusoidal arch attached to a hollow rectangular base, in its (c) stress-free stable state and (d) stressed, second stable state; snapping-through the arch produces a curvature in the initially-flat base, which gives the unit its morphing capabilities. Here, we extend our idea to 2D units – dimpled frames – by introducing arches made of multiple sinusoids attached to a hollow square base; the arch can connect to the base at (e) opposite edges, (g) opposite corners, or (i) opposite edges and corners. (f,h,j) Second stable states of the corresponding units, after snapping.

In a previous study [47], we introduced a one-dimensional, beam-like structural analog of a bistable dimple, that exhibits bistability and allows for tailorable morphing attributes. This unit features a sinusoidal arch and a hollow rectangular compliant base, as shown in its first and second stable states in Fig. 1c,d, respectively. When pushing down on the arch, the base produces enough lateral constraints to cause snap-through buckling and a change of curvature in the flexible base – similar to what we observe in dimpled sheets. However, its one-dimensional geometry prevents the existence of significant coupling between the units, which in turn prevents the system from displaying morphological memory attributes.

In this work, we introduce the idea of *dimpled frame*, a two-dimensional (2D) extension of the base-arch concept; by doing so, we introduce units that are true structural analogs of soft bistable dimples, and that can be potentially made of less dissipative materials like stiff polymers, metals and composites. Our units feature a square base with a square cutout, and sinusoidal arches connected at multiple locations of the base. Specifically, to try and elucidate the origins of memory in arrays of our units, we investigate three types of units: i) the “plus”

unit (Fig. 1e) has an arch composed of two sinusoids, each connecting opposite edges of the base; ii) the "times" unit (Fig. 1g) an arch composed of two sinusoids, each connecting opposite corners of the base; iii) the "eight-leg" unit (Fig. 1i) has an arch that combines those of the plus and times units. We first build our capacity to model these systems by comparing the experimental response of single units, both in terms of force-deformation response and shape change, to numerical reduced-order models based on the discrete elastic rods (DER) framework. We then explore the response of 2D arrays of units both experimentally and numerically, and illustrate the rich morphing capacity of these systems. Specifically, we discover that our structures can achieve mechanical memory, but that this attribute is "feeble" – as it relies on a delicate balance between the intensity of the coupling between units (akin to the distance between dimples in a dimpled sheet), and the nature of the coupling (which differs depending on how the arch is attached to the base). Due to the discrete way in which arch and base are connected, our work offers new insight into the origin of mechanical memory in multistable structures, while introducing a structural concept that can be potentially up-scaled and made of structural materials.

Our article is organized as follows. In Section 2, we introduce the geometry of our units, the fabrication process, and then validate our numerical models with experiments on single units. In Section 3, we explore the behavior of two dimensional arrays of units, focusing on their multistability and mechanical memory attributes in response to different snapping sequences, and build confidence on our ability to model arrays. In Section 4, we present a numerical parametric study on our arrays and identify geometric features that govern the emergence of memory effects. Concluding remarks and ideas for future research are given in Section 5.

## 2. Single units: geometry, experiments, and mechanics

We begin by introducing details on the geometry of our units, the fabrication process, the experimental setup and numerical models. We then validate our models' capabilities to predict the force-deformation response and final shape of single units. These validates models will be of key importance to make prediction on the behavior of arrays of units in the next sections.

### *2.1. Unit cell geometry*

The geometric details of our dimpled frames are shown in Fig. 2. Specifically, Fig. 2a,b,c show the plan views of the plus, times and the eight-leg units, respectively. Each strip of the base and arch has width $w = 5\,\text{mm}$ and thickness $t = 0.5\,\text{mm}$. The base length is denoted by $L_b$ and the horizontal projected length of the arch is denoted by $L_s$. The base lengths $L_b$ used throughout this work vary between 70.7 and 100 mm. For the plus unit, we have $L_s = L_b$; for the times unit, $L_s = \sqrt{2}L_b$. The side views of an arch are shown in Fig. 2c,d in its first and second stable states, respectively. To facilitate bonding to the flat base, the sinusoidal arch has a flat zone

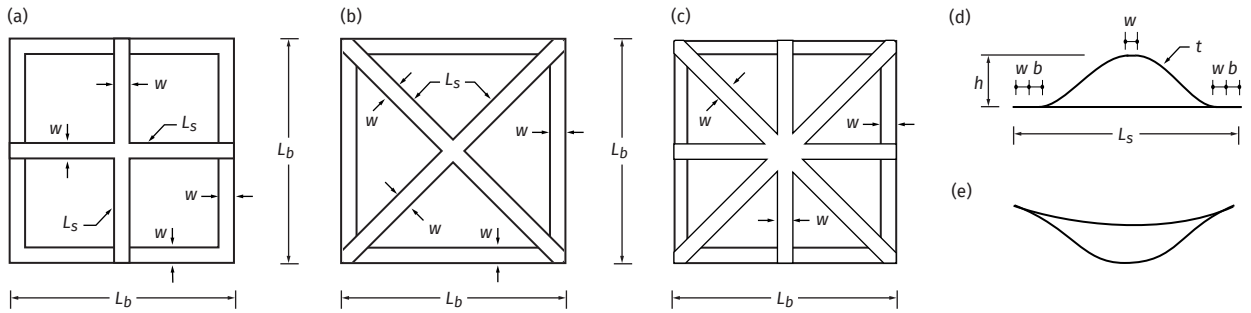


Fig. 2: Unit cell geometry. Plan view of the (a) "plus", (b) "times" and (c) "eight-leg" units, and side views of an arch in these units in its (d) first, and (e) second stable states. The eight-leg unit in (c) can be obtained by superposing the arches in units (a) and (b).

of width $w + b$ (we set $b = w$) on each side. Another flat zone of width $w$ is located at the apex of the arch, to facilitate attachment of the actuation rod during testing. The height measured from the base to the apex of the arch is denoted by $h$. We fabricate each type of unit in three different nominal heights of $h = 10$, 20 and 30 mm.

### 2.2. Fabrication

The fabrication process, inspired by our previous work [47], is illustrated in Fig. 3. We begin with two laser cut parts made of 0.5 mm thick PETG (McMaster-Carr part number 9513K57); the cross shaped part in Fig. 3a is the flat precursor of the sinusoidal arch, while the hollow square in Fig. 3b is the base. To shape the arch

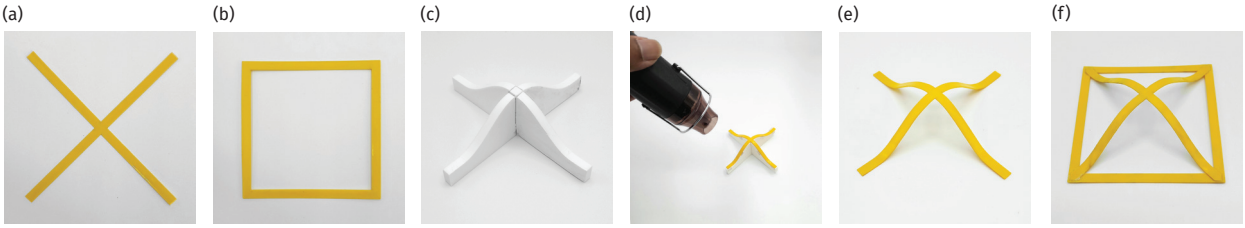


Fig. 3: Fabrication process of one of our units. We begin by laser cutting (a) the arch precursor and (b) the base from a flat 0.5 mm thick PETG sheet. (c) We 3D print a mold of the desired sinusoidal shape and (d) paste the flat arch precursor on the mold by double-sided tape, then heat treat it for about 2-3 minutes; (e) once it cools down, and after removing it from the mold, it retains an arch shape. (f) The sinusoid is then bonded to the base.

precursor into a sinusoid, we use a mold assembled from different bonded parts (several half-sinusoids and one center column), as shown in Fig. 3c. Next we paste the flat cross on the mold via double-sided tape. Then, we heat treat the cross segment using a heat gun (DigiKey part number 133-EC-MINI-ND). Initially, we apply heat uniformly on the entire unit from a few inches away to avoid any localized heat concentration, then we focus on treating each leg separately and apply heat via rotatory movements to avoid unwanted warping. After applying heat, we let the cross cool and then gently remove it from the mold. If the heat treatment is done properly, the arch should retain its sinusoid shape as in Fig. 3e. Finally, we bond the flat base to the arch using cyanoacrylate glue and the resulting unit is shown in Fig. 3f. A properly made unit should feature smooth sinusoidal arches free of kinks and warping, and a base that is free of camber when glued to the arch – an indicator of the absence of prestress in the unit.

### 2.3. Experimental setup

To quantify the mechanical response of the units, we perform compression tests in an universal testing machine (UTM, Instron 68FM-100) by applying a downward displacement at the apex of the arch and reading out the force along the same direction. To capture the full response, we apply displacement beyond the second equilibrium point (if present). Fig. 4a shows the experimental setup. To actuate each unit, we use a T-shaped actuation rod as shown in Fig. 4 with rubber pads to facilitate gripping by the UTM. The end of the actuation rod is glued to the apex of each unit through a circular acrylic piece of 5 mm diameter, as shown in Fig. 4b, to ensure consistent contact during the entire loading and unloading process. We apply displacements at a rate of 0.5 mm/s to ensure quasi-static loading. The units are mounted on the setup through four slotted cylinders (McMaster-Carr part number 97161A199); each corner of the base is inserted all the way to the inner wall of the cyliders, and bonded using hot glue as shown in Fig. 4c. Each cylinder rests on two support arms made of acrylic, which have an open slot for the cylinder to slide in, as shown in Fig. 4d. The slots have openings that are just enough to accommodate low-friction horizontal movement and rotation of the cylinders, while preventing vertical movement, thus providing roller-like supports to the base. Each support arm is bonded to the corresponding support wall, and the wall is connected to the base plate using angle brackets. A complete set of drawings to laser cut a 20 mm high unit of the times type, 3D print the molds, and fabricate the experimental setup is shown in Fig. D.16.

### 2.4. Numerical model

Our structures are effectively made of ribbons, whose thickness-to-width-ratio is 10:1. Due to absence of large localized deformations or extreme axial-twist coupling, we choose to model them as 1D rods. To do so, we use an in-house MATLAB-based modeling tool based on Discrete Elastic Rods (DER) – a discrete differential geometry modeling technique originally proposed by Bergou et al. [48, 49]. Details on our DER implementation are reported in Appendix A. DER is a well established simulation technique in computer graphics [48–53] due

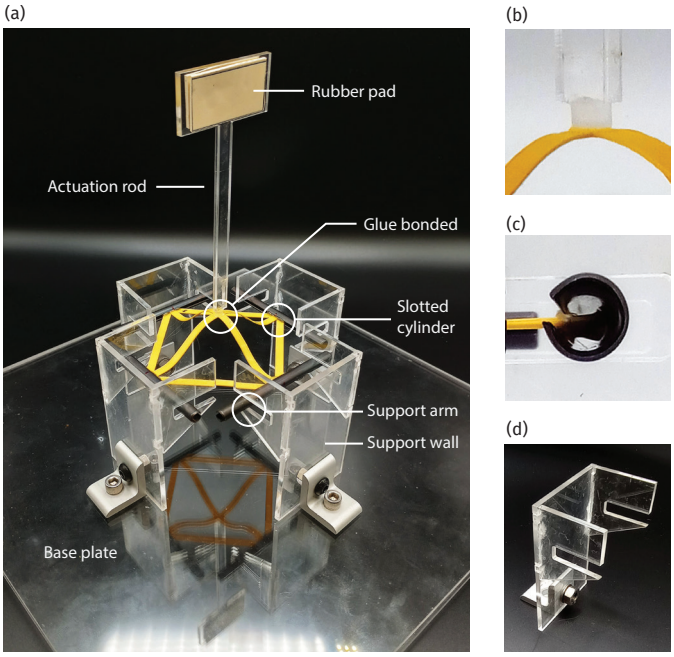


Fig. 4: Experimental setup for the uniaxial test of single units. (a) A times unit is mounted on the test setup, where the apex of the arch is glue-bonded to a T-shaped actuation rod made of acrylic, as shown in the close-up in (b). The flange of the actuation rod has rubber pads on both sides to facilitate gripping by the UTM. Each corner of the base is inserted all the way into a slotted cylinder, and bonded with hot glue as shown in (c). Each cylinder rests between two support arms extended from a vertical structure made of acrylic, as shown in (d); this structure, by allowing the cylinders to translate horizontally but not vertically, provides a roller-like boundary condition.

to its efficiency. As DER has the capability to capture all basic deformation modes (axial, bending and twisting) in addition to bending-twisting coupling, it has gained traction in the mechanics community to simulate flexible structures undergoing large deformations, and to tackle problems involving cable deployment [54], fluid-soft solid interactions [55], soft robot locomotion [56], contact friction [57], buckling [58, 59], ribbon mechanics [60, 61], and gridshells [62].

Unlike the traditional finite element method, which can easily handle complex structural assemblies, the original DER formulation can only simulate disconnected rods. To overcome this limitation, several modifications have been proposed in the literature [63–67]. One of these uses an implicit penalty approach by inserting a stiff spring [47, 66] between two junction nodes of two intersecting rods, and by adding penalty terms in the stiffness matrix and in the internal force vector. This approach only allows coupling of the translational degrees of freedoms ($x$, $y$ and $z$) between the connected nodes of two rods, and cannot be used to account for bend-twist coupling at the joint of two rods as required in our work. To overcome this limitation, we resort to a coupling strategy pioneered in Ref. [67], where three-noded linker rods are inserted between the rods to be connected. The linkers themselves, whose properties are identical to those of the other rods, ensure the occurrence of bend-twist coupling (because the linkers themselves couple these modes of deformation). In addition, penalty terms are added via trial-and-error to ensure that the connection behaves rigidly and prevents relative motion between the rods. These penalty terms needs to be large enough compared to the stiffness of the connecting rods, but cannot be too large to avoid numerical singularities.

Fig. 5 shows the schematic of the DER model for a times unit. The base has dimensions $L_b \times L_b$, and the arches have height $h$. The base is modeled with four rods and the arches with two rods (four rods in the case of the eight-leg unit). We apply a downward displacement $D$ at the apex of the arch. The four corners of the base have planar roller supports (which can only resist forces in the $z$ direction), and the apex of the arch features a vertical guide that only allows motion in the $z$ direction. To properly couple various rods, we placed linker rods at each joint. When placing linkers, it should be noted that the edge vectors of the regular rod and the corresponding linker rod must point in the same direction; in other words, the positive directions of the torsional

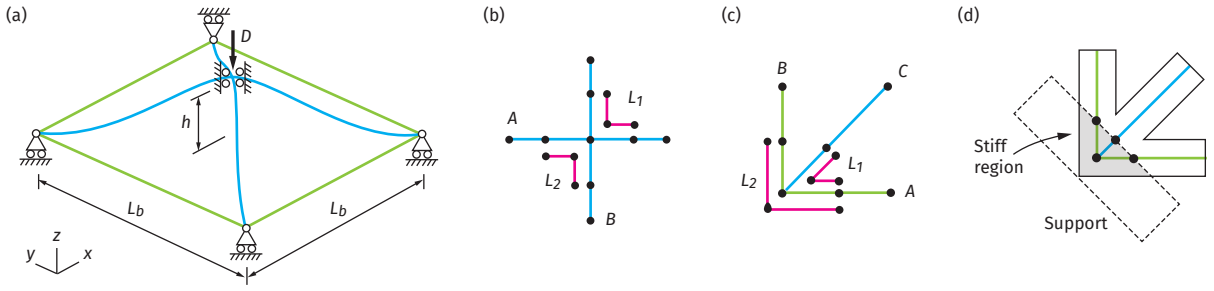


Fig. 5: Numerical modeling approach for single units, using discrete elastic rods (DER). (a) Four straight rods are used to model the square base, and sinusoid-shaped rods are used for the arch structure. Horizontal rollers at the corners, and a vertical guide at the apex of the arch, replicate the boundary conditions of the experiments. (b) Detail of the connection between the arches at the apex, featuring linkers between rods [67]. The arch rods $A$ and $B$ are connected by two linkers $L_1$ and $L_2$. (c) Detail of a corner of the unit, where one linker $L_1$ connects base rod $A$ and arch rod $C$, and another linker $L_2$ connects the two base rods $A$ and $B$. (d) The slotted-cylinder support in the experiment entraps a region of the base and the sinusoid, making it rigid; this is accounted for in the model by using stiffer rod elements in that region.

degree of freedom must be the same for the rods being joined. Fig. 5b shows a detail of the apex of the structure, where rods $A$ and $B$ are connected by two linkers $L_1$ and $L_2$ at opposite corners. Linkers cannot be placed on the other two corners, since doing so would cause the rod and corresponding linker edge to have negatively-related torsional degrees of freedom. Fig. 5c shows the details of a corner where linker $L_1$ connects the arch rod $A$ and the base rod $C$, and another linker $L_2$ connects the base rods $A$ and $B$. For the same reason stated above, it is not possible to put linkers between the arch rod $C$ and the other base rod $B$. Fig. 5d shows the modeling detail of a corner. When preparing our units for experiments, we push the base corners all the way into the slotted cylinders; in turn, due to the presence of solidified glue inside the cylinders, the portion of base and arch inside the cylinder behaves almost rigidly. This is accounted for in the model by stiffening the linkers at the corners.

In our models, we set the material properties of PETG to be: Young's modulus $E = 2.2 \times 10^9$ Pa, density $\rho = 1.3 \times 10^3$ kg/m$^3$ and Poisson's ratio $\nu = 0.38$ [47]. To correctly capture torsional deformations in our beams, we also need a shear modulus $G$, which we calculate from the Young's modulus and assuming a Poisson's ratio $\nu = 0.38$, and a polar moment of inertia for the cross section. As our beams are ribbon-like, the polar moment of inertia for a rectangular cross section does not correctly capture their torsional behavior; we mitigate this issue by introducing a torsional stiffness modifier $J$, whose value is identified via trial-and-error by comparing experimental and numerical deformed shapes, as discussed in Section 2.6 and Appendix B.

### *2.5. Force-deformation response of single units*

In Fig. 6, we compare numerical and experimental force-deformation responses – the first step in the validation of our models. The plots are grouped by type of unit (times, plus, eight-leg) in each column, and by arch height in each row. All units tested have base length $L_b = 70.7$ mm. The upper 3×3 panels in the figure show force-deformation comparisons for nominal height $h = 10$, 20 and 30 mm, for each unit type. For each mechanical test, we record the force-deformation during loading (continuous blue line) and unloading (dashed blue line). We test three samples of each height and unit type: lines represent the average of three tests, while shaded areas indicate standard deviations. The numerical responses for loading and unloading are overlaid as continuous and dashed magenta lines, respectively. The lower 1×3 panels of Fig. 6 show the internal energy vs. apex displacement for a $h = 30$ mm height for each unit type, to explain their mode of deformation. The total energy in these plots is shown in black, and decomposed into bending and twisting contributions, represented by dark and light gray lines, respectively. The stretching energy is almost zero for all units and not reported in our plots. With an eye towards our array simulations in Section 3, it is worth to note that some units that do not seem bistable in Fig. 6 are instead bistable if we remove the constraints imposed by the roller-like boundary conditions and actuation rods. Yet, introducing these realistic constraints is necessary to validate our simulations against experiments.

At a first glance, it is clear that the times units, whose results are shown in Fig. 61-d, results in the most well-defined responses, free from any experimental noise and numerical "jumps". Their loading and unloading paths are almost identical, and the numerical and experimental results match with great accuracy. For an arch

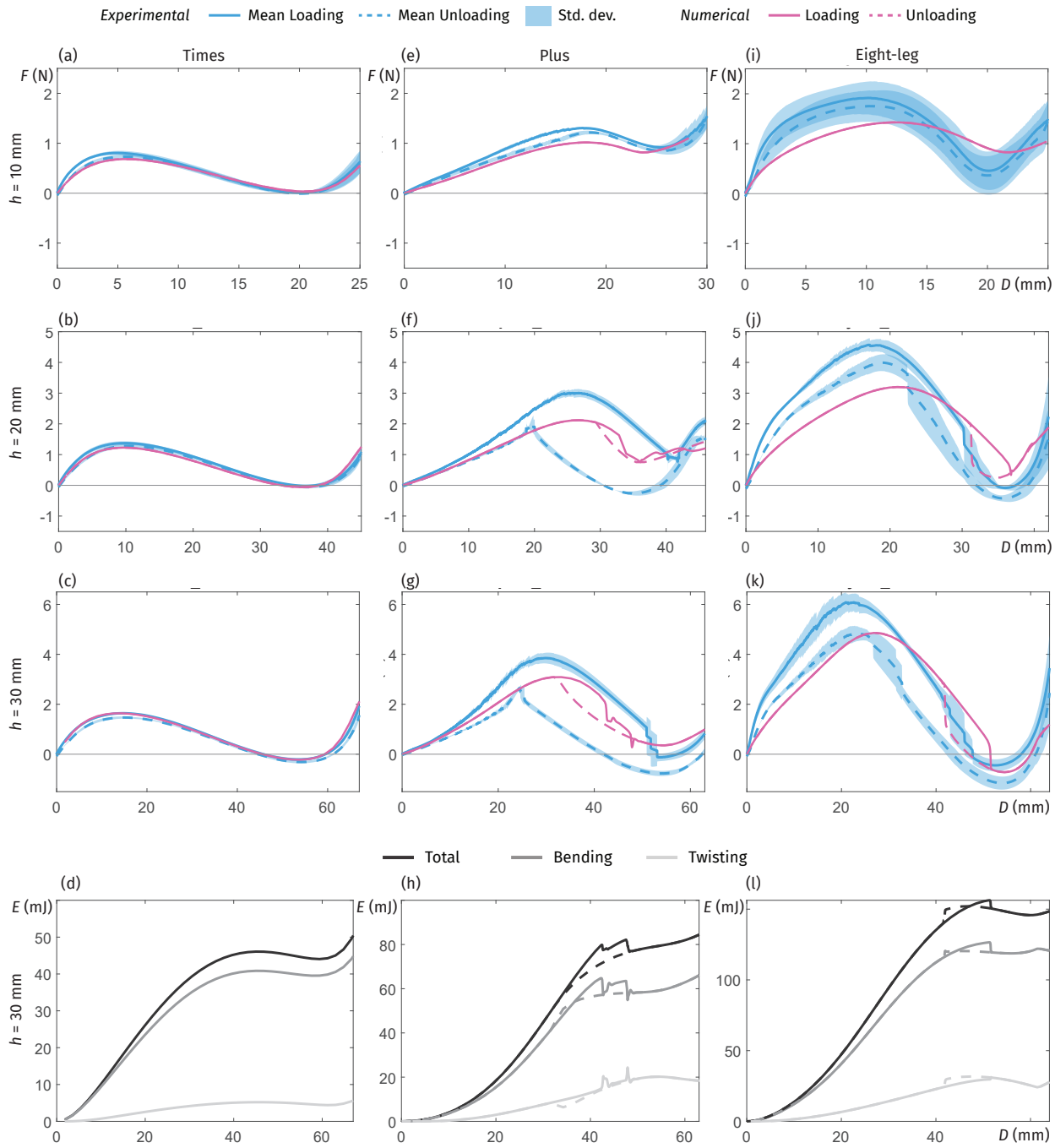


Fig. 6: Response of single units. Each column represents a unit type (times, plus and eight-leg), and each row represents a specific height of $h = 10$ mm, $h = 20$ mm and $h = 30$ mm. The top 3×3 panels show force-deformation curves. For the experiments, we report the loading (continuous blue) and unloading (dashed blue) responses, where each curve represents the average of three tests, and each shaded area represents the standard deviation. Numerical responses for loading and unloading are shown as continuous and dashed magenta lines, respectively. The bottom $1 \times 3$ panels show internal energy plots from the simulations of the units with $h = 30$ mm height. The total energy (black line), is further decomposed into bending (dark gray) and twisting (light gray) energy; the stretching energy is negligible.

height $h = 10\,\text{mm}$, we can see that times units are barely bistable: the force deformation response from the experiments barely creeps into the negative force region, while the numerical curve remains above the zero force

axis. The response of taller units of the same family, in Fig. 6b,c show that, as the critical force rises, the curve also dips more into the negative force region, making the unit more bistable. Fig. 6d shows the total internal energy and its decompositions into bending and twisting energy for the times unit with $h = 30$ mm. We observe that, for these units, the primary deformation mode is bending, with low twisting deformation. The peak and the dip of the total energy in this figure correspond to the unstable equilibrium and second stable state from Fig. 6c, respectively.

The second column of plots, in Fig. 6e-h, shows that the plus units require more force to reach the same level of displacement as the times ones. Compared to the times units, the plus ones are less bistable, with the experiments showing some bistability as the arches get taller. The numerical results for all plus units under-predict the critical forces, but the curves remain confined within the experimental loading and unloading paths. Interestingly, the loading and unloading paths are significantly different for the 20 mm and 30 mm cases, as shown in Fig. 6f,g, respectively. Different equilibrium paths for shallow arches are also reported in Refs. [68–74]. We believe that this phenomenon is due to a secondary snapping that takes place within the units as a result of large twisting deformations. In fact, as shown in Fig. 6h, the twisting energy for these units now on the same order of magnitude as the bending one. The presence of secondary snapping is likely associated with the vertical jumps observed in both numerical and experimental responses of Fig. 6f,g. Visual inspection of the experimental videos (see Appendix E) shows that these jumps correspond to sudden changes in the base shape from bent with low twist to straight with high twist during loading, and vice versa during unloading.

Finally, we discuss the response of the eight-leg units, as shown in Fig. 6i-l. We notice that the experimental standard deviations are larger compared to the other units, which we believe is due to the fact that more legs imply more likelihood of imperfections. As the arch height increases, both the standard deviations and the differences between numerical and experimental results decrease. Interestingly, the critical force of these units are similar in value to the sum of the critical forces of the times and plus units. Additionally, we also observe some global resemblance with the times and plus responses: the initial steep slope in the eight-leg units resembles that of the times units, while the vertical jumps are akin to those in the plus units. These units also exhibit different equilibrium paths in loading and unloading, and they also have a large twisting-to-total energy ratio.

### *2.6. Deformed shapes of single units*

We now shift our focus to a comparison between experimentally-reconstructed and simulated shapes of our units in their second stable states – the second step in our model validation process, and a very crucial one to be able to numerically predict the shapes of our arrays. Results of this comparison are presented in Fig. 7. For this analysis, we fabricate one specimen per type, with base length $L_b = 100$ mm and height $h = 30$ mm; these parameters are chosen to ensure bistability of the units. Before scanning, we prepare each specimen by drawing evenly spaced dots along the centerline of each strip, as shown in the first row of Fig. 7. Next, we scan the second stable state of each unit using an EinScan-SP 3D scanner, and extract the coordinates of the marked points. From a modeling perspective, we apply boundary conditions as indicated in Fig. 5a, without additional constraints at the corners of the base. We then load the units beyond their second equilibrium and release the load (leveraging the dynamic capabilities of our code), allowing the units to settle in their second stable states. The point clouds representing the center lines of all base strips and arch beams in both experiments and models are shown in the lower $3 \times 3$ panels in Fig. 7, where the second row shows isometric views, the third row shows top-down views ($xy$ plane), and the fourth row shows side views ($zx$ plane) of each unit. For a better comparison, we translate the the point clouds so that the arch apexes coincide between model and experiment.

Fig. 7a-d show that, for the times unit, the numerical model can predict the second stable state with great accuracy. The arches stay diagonal and cause the corners of the base to move towards the center of the unit in Fig. 7c; in turn, this causes the base edges to curve outwards. Some deviations between model and scan are visible near the base-arch attachment points in the side view in Fig. 7d, but they are very minimal. Fig. 7e-h show instead the results for the plus unit – that displays the largest deviations between model and experiment. These deviations are due to a loss of symmetry in the snapped physical unit, shown in Fig. 7e, which causes a couple of base edges to twist significantly and the others to bend without much twist; on the other hand, the model shows that the base should remain symmetric after snapping, maintaining an almost-square shape as shown in Fig. 7g. We believe that the reason for this large discrepancy is due to the complex deformation imparted by the arches onto the base in this particular unit, that involves significant twisting and secondary snapping of the

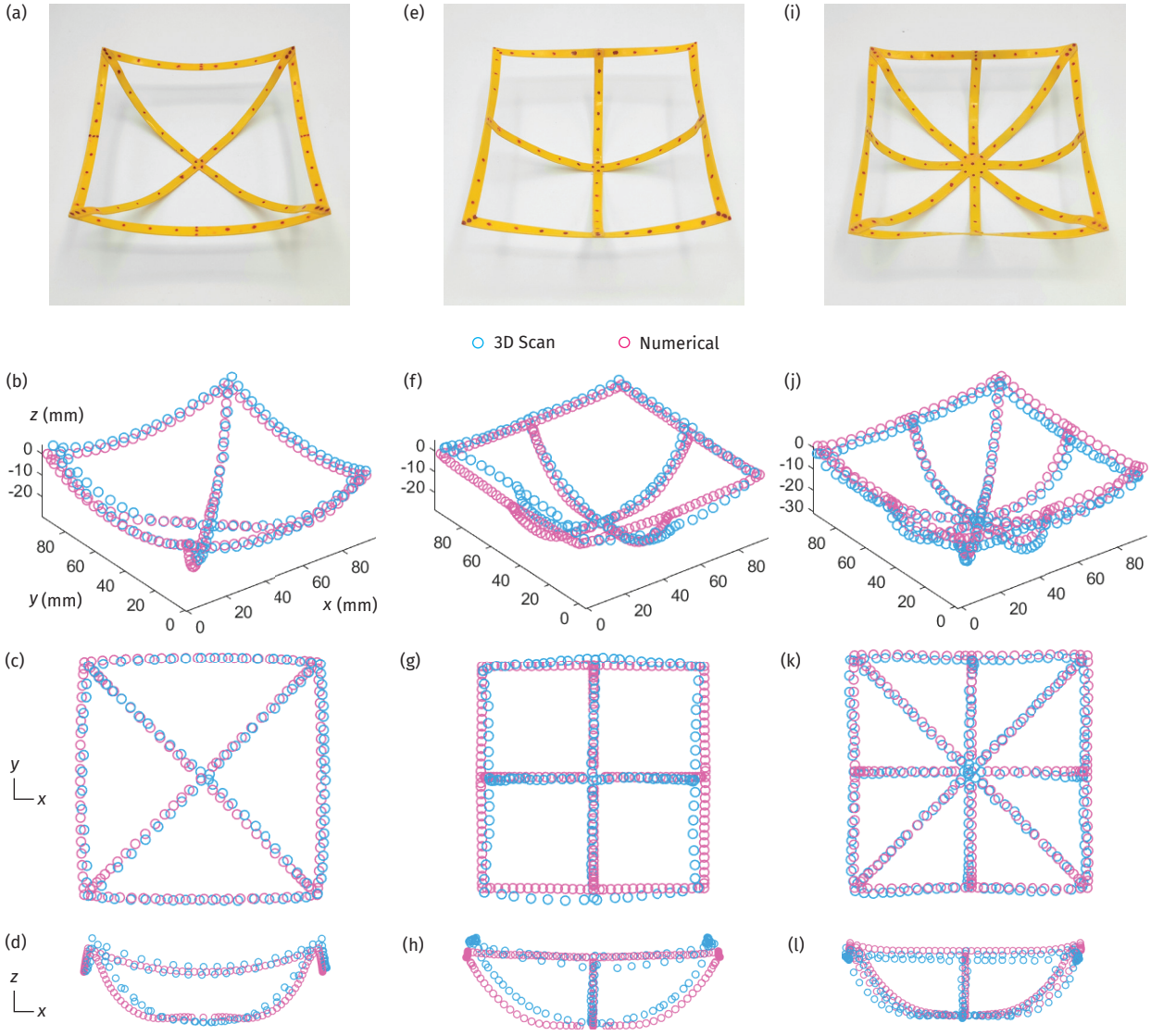


Fig. 7: Shape-morphing of single units. Each column illustrates, from top to bottom: a photo of the unit in its second stable state; the comparison between numerical and experimentally-reconstructed shapes in isometric, top-down and side views. Blue point clouds are obtained from the physical samples via 3D scanning (with scanning points located along the beams' centerlines), while magenta point clouds represent the numerical predictions of the second stable states. Results for the: (a)-(d) times, (e)-(h) plus, and (i)-(l) eight-leg units.

base edges, from highly bent to highly twisted (as discussed in Section 2.5). In turn, fabrication imperfections could cause this secondary snapping to only happen in some base edges, as we see from our results. Results for the eight-leg unit are shown in Fig. 7i-l and indicate that the base edges undergo significant twisting and more bending than in the plus units. From Fig. 7s, we can see that symmetry is maintained in this unit, thanks to the presence of diagonal arches that act as bracing for the system and counteracting potential imperfections in the parallel arches. From the side view in Fig. 7l, we see that the base lies mostly flat except near the corners, and that the angles of the arches match pretty well between the scan and the model.

## 3. Two-dimensional arrays: multistability and mechanical memory

After learning about the behavior of single cells, and building confidence on our capacity to model these structures, we move to 2D arrays, i.e., planar tilings of units. Specifically, we focus on $3 \times 3$ arrays of each unit type (times, plus and eight-leg) as this size is sufficient to capture complex morphing scenarios at a contained computational cost.

### *3.1. Challenges in modeling arrays*

Efficiently modeling arrays of units requires us to parallelize our codes. For efficient parallel computation and to avoid bottlenecks, it is important for all CPU cores to handle tasks involving comparable execution time. Given that constructing the stiffness matrices is the most time consuming step in our simulation, comparable execution time among cores can be achieved by modeling arrays using assemblies of similarly-sized rods. This idea is illustrated in Fig. 8 for the base of a $1 \times 3$ array. If our goal is to model the base in Fig. 8a, we can either model the long edges of the base as single rods as in Fig. 8b or as multiple rods as in Fig. 8c. The latter case is more suitable for parallelization, as all rods will have comparable lengths and comparable numbers of nodes.

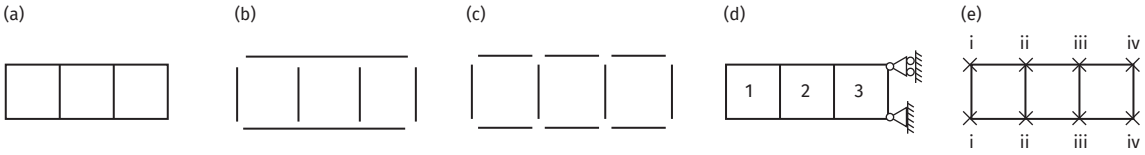


Fig. 8: Numerical modeling approach for the sequential snapping of arrays of units. (a) Schematic of a 1×3 array. (b) An inefficient modeling approach where the base is modeled using two long rods and four short rods, resulting in a imbalance in the number of nodes per rod that would yield inefficient parallel computations. (c) The optimized modeling approach used in this work, with rods of comparable size to ensure a balanced computational load across CPU cores. (d) A target sequential snapping order for the units in the array, with its final boundary condition. (e) The process to achieve sequential snapping: step 1, all base joints marked by crosses are pinned; step 2, all units are snapped simultaneously while the base joints remain pinned; step 3, pins are released in a i, ii, iii sequence, corresponding to the desired snapping order, allowing the global shape to change as the supports are released. To comply with the desired, final boundary conditions in (d), the pins marked by iv become the final boundary conditions.

Another modeling challenge relates to the logistics of snapping units in specific sequences – something that is needed to probe the mechanical memory attributes of the arrays. As we snap each unit of an array, its global shape changes significantly, making it challenging to know how to apply forces to snap subsequent units. Additionally, the particular unit we are snapping must be temporarily supported, further complicating the modeling process. To address this issue, we adopt a technique introduced in Ref. [41]and illustrated in Fig. 8d,e. As an example, we assume that the units in Fig. 8d need to be snapped in the 1-2-3 order, with final boundary conditions also shown in the same figure. We achieve this snapping sequence by a series of three steps. First, we pin all the base joints as shown by the cross markers in Fig. 8e. Second, we snap all units at the same time, while keeping the base joints pinned. Third, we release the supports according to the desired snapping sequence. This process can be best modeled using a dynamic implicit solution procedure, where we solve our equilibrium equations iteratively at each time step, as discussed in Appendix A. Choosing the right value of damping is key to limit the oscillations of the released units, as discussed in Appendix C.

### *3.2. Morphing shapes and memory*

We now focus on the analysis of 2D arrays, concentrating on their morphing capacity and memory attributes. For each type of array (made of times, plus or eight-leg units), we study two different base geometries by altering their inner strip widths – thus altering the distance between units and, consequently, their coupling. Specifically, we consider single-width bases, where all strips have 5 mm width, and double-width bases, where all inner strips have 10 mm width (while we keep the external strips to a 5 mm width). Note that the double-width array is a more proper planar tiling of the unit, since it is obtained by translating the unit of an amount equal to the unit base length $L_b$.

We begin with arrays of times units, where we set $L_b = 90\,\text{mm}$ and the arch height to $h = 30\,\text{mm}$. The undeformed state of the double-width array is shown in Fig. 9a. In Fig. 9b, we show a stable state of the array

when snapped according to the actuation sequence shown in the inset of the figure. This sequence is chosen to try and achieve a global, cylindrical deformed shape that curls about the $v$ axis. Unexpectedly, the global shape is more symmetric and bends equally about both $u$ and $v$ axes. We observe the same behavior when we rotate the snapping sequence by 90 degrees, as shown in Fig. 9c. We conclude that this double-width array of plus units has a single stable shape and no memory when all units are snapped – as all snapping sequences yield the same global shape. To model the same array, we consider the rod arrangement in Fig. 9d, which also shows the support

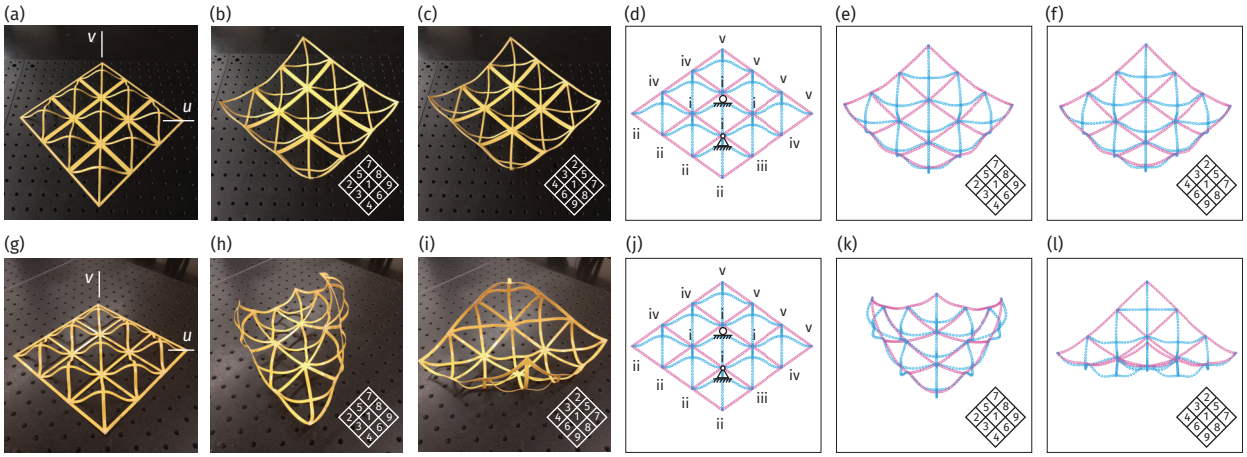


Fig. 9: Morphed shapes and memory attributes of the "times" arrays. (a) Undeformed state of the double-width array with diagonal axes $u$ and $v$ aligned with the arch strips. (b,c) Experimentally observed stable shapes of the double-width array under two different snapping sequences (shown in the insets), both designed to favor cylindrical bending about a single axis. Despite demonstrating different intermediate configurations, both sequences result in a symmetric global deformation about both $u$ and $v$. (d) Support release sequence corresponding to (b), where multiple units are released together to accelerate the process. (e,f) Numerical models of the configurations in (b,c), confirming the experimentally observed symmetry. (g) Single width times array exhibiting the cylindrical bending shown in (h,i), with axes determined by the first fully-snapped diagonal. Numerical simulations (k,l) confirm these results.

release sequence for the snapping sequence in Fig. 9b, and the final boundary condition after all temporary pins are released. Even though the snapping sequence in Fig. 9b has nine steps, we speed up the process by releasing some groups of units together (e.g., units 2,3,4, in the snapping sequence are released in step (ii) of the support release sequence). The simulated deformed shapes in Fig. 9e,f correspond to the experimental shapes in Fig. 9b,c, respectively. We see that the numerical model behavior matches that of the physical samples, with equal bending about the $u$ and $v$ axes.

To try and achieve global multistability and memory, we fabricate the single-width array in Fig. 9g. In this case, the same snapping sequences as in the double-width array produce different shapes: the array bends about the $v$ axis when snapped in the sequence of Fig. 9h, and about the $u$ axis in Fig. 9i. As the array bends about its diagonals, we label these shapes as diagonally bent. Our models in Fig. 9k,l predict the same behavior. While not a very exciting one, this is an example of global multistability and mechanical memory, as the array possesses two distinct stable states when all units are snapped. Interestingly, we observe that the bending axis of the global shape is always determined by the first diagonal to have all three of its units snapped.

We now move to arrays of plus units, where we set $L_b = 90\,\text{mm}$ and $h = 30\,\text{mm}$. A fabricated double-width array of this type is shown in Fig. 10a. When we snap the units as in the inset of Fig. 10b – basically, a sequential snapping along the $y$ axis – we obtain a global cylindrical shape that also bends about the $y$ axis. When we rotate the snapping sequence by 90 degrees, the array bends about the $x$ axis as shown in Fig. 10c. We conclude that this array is multistable and has memory like the single width times array, but its stable global states bend about an axis that runs parallel to the base strips – which we refer to as orthogonally bent. What is surprising is that, for these units, we do not need to resort to a single-width base to achieve memory. This stronger coupling between plus units could come from the fact that, for the same base width and arch height, the arches in the plus units are less shallow than the times ones, and therefore bound to produce more base deformation. The numerical model of this array, its snapping sequence, and its shapes in response to the actuation sequences in Fig. 10b,c,

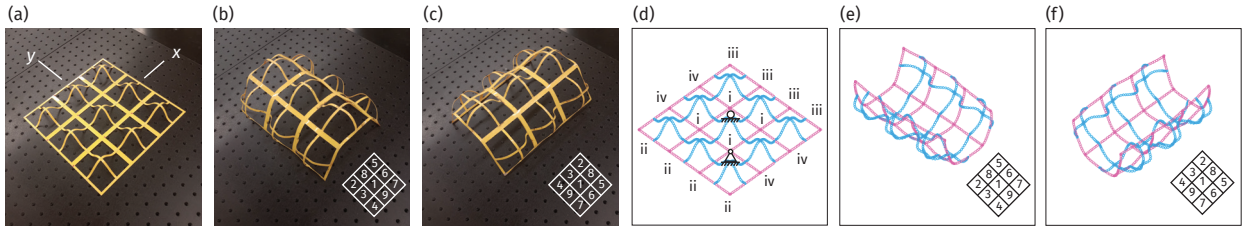


Fig. 10: Morphed shapes and memory attributes of the "plus" array. We concentrate on a specimen with double-width base; no stable morphed configuration is found for the single-width base, as shown in our supplementary videos of Appendix E. (a) Undeformed state with reference axes $x$ and $y$ aligned with the arch strips. (b) Experimental deformation resulting from a sequential snapping along the $y$ axis (inset), producing a cylindrical surface bending about $y$. The images shown in (b,c) are upside-down for easier visualization. (c) Rotation of the snapping sequence by 90° yields bending about the $x$ axis. (d) Support release sequence used in the numerical model for (b). (e,f) Numerical deformed shapes corresponding to (b,c).

are shown in Fig. 10d-f. We can see that the model predicts the deformed shapes very well.

For consistency with the times arrays, we also fabricate and test a single-width plus array; upon applying the same snapping sequences as in Fig. 10b,c, we observe that these same global shapes are no longer achievable: snapping the neighbor of an already-snapped unit causes it to revert to its original state. We show this behavior in one of our supplementary videos listed in Appendix E. We think this happens because because the single-width base is not wide enough to bend across its width and to allow the connected sinusoids to have the required angle that keeps them snapped. The same behavior is also observed in our simulation where, after pinning all base corners, snapping all nine units and releasing the supports, the units unsnap and the whole array eventually returns to its original state.

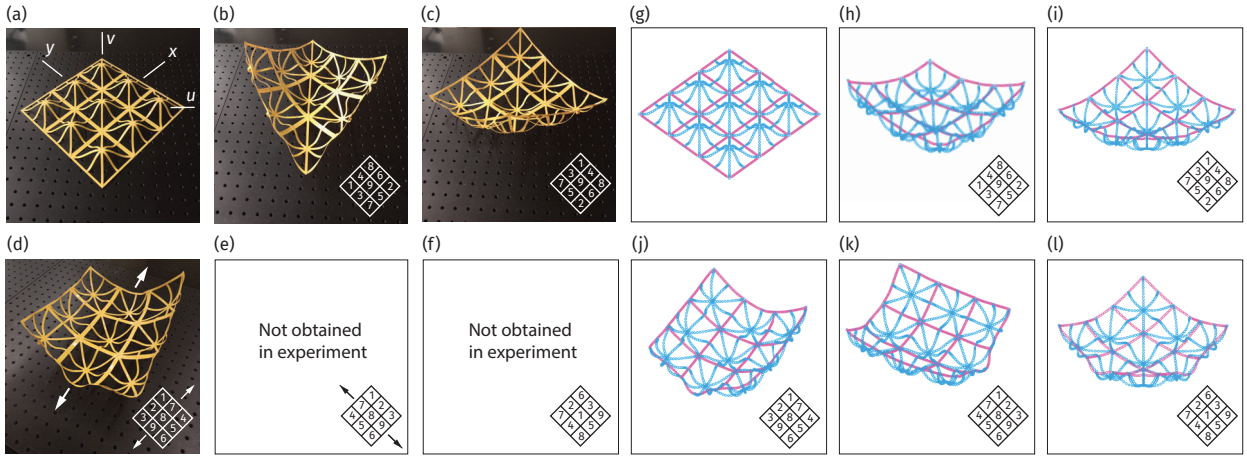


Fig. 11: Morphed shapes and memory attributes of the "eight-leg" array. We concentrate on a specimen with double-width base; tests with the single-width base show no morphing response since neighboring units fail to remain snapped. (a) Undeformed state with two sets of reference axes: $x, y$ parallel to the base strips and $u, v$ parallel to the diagonals. (b,c) Experimental diagonal bending states about axes $v$ and $u$, achieved with the same snapping sequences as the times array; these stiff, bistable states can be switched between and are reproduced by simulations in (e,f). (g) Orthogonal bending mode analogous to the plus array, requiring additional edge snapping (inset) to lock the base into a low-energy state. This configuration is weaker and more fabrication-sensitive, preventing experimental realization (h), but obtained numerically about both $x$ and $y$ axes in (j,k). (i) Experimental attempt at a radially symmetric state, left empty due to instability, while (l) shows the corresponding numerical result from the indicated snapping sequence.

Finally, we move on to the arrays of eight-leg units, which are characterized by a slightly larger base length $L_b = 100\,\text{mm}$, and by $h = 30\,\text{mm}$. We concentrate on a double-width array, as we observe that the single-width array returns to its undeformed state for all snapping sequences. For reference, in Fig. 11a, we label $x, y$ the axes parallel to the base strips, and we label $u, v$ the axes parallel to the diagonals of the array. As arches in these units have both parallel and diagonal sinusoids, we expect eight-leg arrays to feature attributes of both the

plus and times arrays. As shown in Fig. 11b,c, the double-base array indeed exhibits diagonal bending about both $u$ and $v$ diagonals, for the same snapping sequences that produced similar shapes in the times arrays. These experimental shapes are confirmed by simulations in Fig. 11e,f – albeit the model shows smaller deformations than the specimen. The eight-leg array also exhibits orthogonal bending, like the plus array, as shown in Fig. 11g, in which the structure bends about the $x$ axis. It is to be noted that obtaining this shape requires snapping of two edges, as shown by the arrows in Fig. 11g, in addition to actuation of the units according to the indicated sequence. This seems to indicate that these shapes cannot be achieved so easily – an aspect that is confirmed by the fact that, in our experiment, we could not achieve a stable shape featuring orthogonal bending about $y$, as shown in Fig. 11e. In our model, though, we can achieve both orthogonally bent states without additional manipulation of the structures' edges, as shown in Fig. 11j,k. In the model, and similarly to what has been observed for dimpled sheets, we also discover a radially-symmetric shape (that has symmetries about the $x, y, u, v$ axes), shown in Fig. 11l. Unfortunately, this highly symmetric shape seems to be the least robust, and could not be achieved in our sample.

## 4. Parametric study and mechanistic considerations

From the exploration of different arrays of equal and double base width, it is clear that the geometry of the units and the distance between them plays a role on the appearance of multistability and mechanical memory. To further probe the role of various geometrical parameters – now that we have confidence on the capacity of our models to predict the behavior of physical arrays – we conduct a numerical parametric study on the behavior of the arrays as a function of strip width $w$ and arch height $h$. The first row of Fig. 12 shows the target global stable shapes we are looking for in each array type, and the bottom row shows the parametric maps for the corresponding target shapes. In each map, we vary the strip width $w$ along the horizontal axis and the arch height $h$ along the vertical axis. A black box boundary in the map indicates the parameters used to obtain the shape shown above each map. The dark gray blocks in the map represent the cases where the array is not stable (the arches snap back to the original state after support release) and the light gray blocks represent cases in which the target shape is not achieved (it gives another shape which doesn't exhibit memory). The colored blocks are the cases where the target shapes are achieved. A circle inside the blocks indicates the behaviors we verified experimentally in Section 3, while a cross indicates those cases that we could not verify for the corresponding physical specimen.

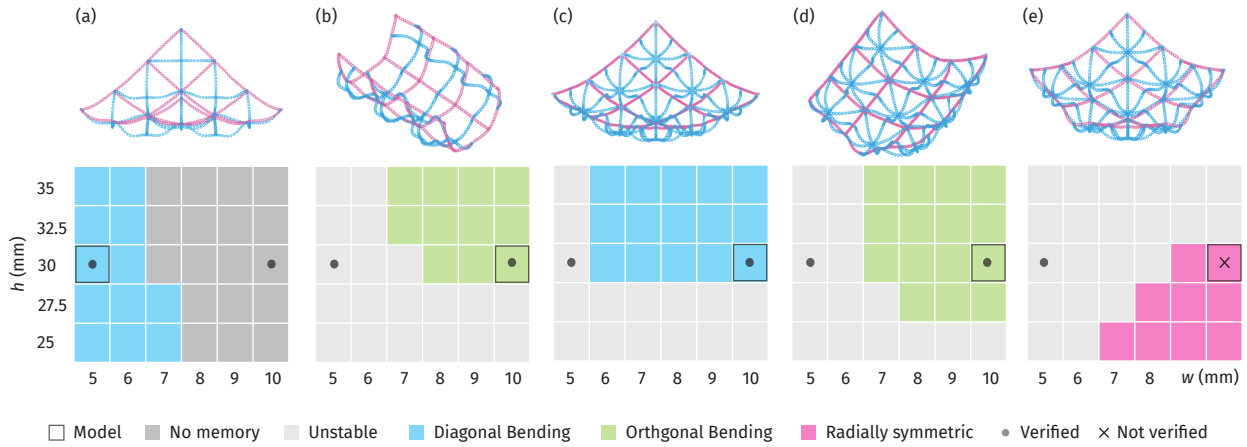


Fig. 12: Numerical parametric study on the link between memory and geometric attributes of the cells. Parametric map of strip width $w$ vs. sinusoid height $h$ for: (a) diagonal bending in the times array; (b) orthogonal bending in the plus array; and (c) diagonal, (d) orthogonal, and (e) radially symmetric states in the eight-leg array.

For the times array, the map shown in Fig. 12a indicates that the diagonally bent stable shapes, and thus all memory attributes, disappear as the strip width gets larger; in such cases, all sequences result in a single shape that looks like Fig. 9b, with no dominant diagonal bending. This behavior can be ascribed to how the arches are

attached to the base. In fact, units interact through their corners, where the arches are attached, and not through the base strips; thus, as base strips get wider, the only consequence is that they become stiffer and diminish the system's tendency to bend significantly about the diagonal axes.

Moving to the plus array in Fig. 12b, we observe the opposite behavior with respect to the times array: the target shape is only achieved for base strip widths above 7 mm. This is consistent with what we observe experimentally in Fig. 10, and is due to the way these units deform when snapped. As discussed in Section 2.6, snapping causes significant twist of the base strips; if these are too narrow, snapping the neighboring unit makes the base strips very stiff in bending about their axes, and causes them to twist back, potentially snapping the previous unit back to its original shape. This behavior hints to the fact that, in our dimpled frames, more coupling between units is not a universal recipe for memory. This sets our structures apart from dimpled sheets, where less distance between snapping units always causes more pronounced global deformed shapes [42]. We also observe that there is a height threshold (30 mm) below which we are not able to achieve the desired shape, likely due to a loss of bistability of each unit.

Finally, we discuss our parametric results for the eight-leg array shapes shown in Fig. 12c-e. The map for the diagonal bending state is shown in Fig. 12c and, interestingly, it differs from the map for the similar shape achieved by the times array, in Fig. 12a. This hints to the fact that the orthogonal legs – those also present in the plus arrays – are the dominant ones in the eight-leg unit. This is also visible from the maps of the orthogonally bent and radially symmetric shapes in Fig. 12d,e, where we can see that these shapes can only be achieved if the base strips are wide enough. Specifically, the map for the orthogonally bent shape shown in Fig. 12d is similar to the map for the same shape of the plus array, in Fig. 12b. The radially-symmetric shape, whose map is shown in Fig. 12, exists over a parametric region that barely overlaps with those of the other stable shapes of the same array. For low $h$ and large $w$, the radially-symmetric shape becomes the only one available – meaning that the system loses its memory and all snapping sequences lead to the same final shape (as in the no-memory region of the times array in Fig. 12a). The only parameter sets over which all shapes coexist are $\{w,h\} = \{(9,30),(10,30)\}$: this is the region where memory attributes are most pronounced and the eight leg array can achieve five distinct shapes (two diagonal bending, two orthogonal bending and one radially symmetric states) depending on the snapping sequence. The feeble nature of these memory attributes is remarked by the fact that, even though our eight leg specimen in Fig. 11 was supposed to feature five stable states, we were only able to access three of them.

## 5. Conclusions and outlook

In this work, we extend our concept of shape retaining morphing structure based on locally-snapping, bistable unit cells [47] by introducing two-way morphing effects – which better capture the response of the soft dimpled sheets our structures are inspired by. We introduce a fundamental "arch and base" unit (with arches attached to the base in different ways), illustrate how to fabricate them, evaluate the units' load-deformation response through experiments, and compare the results to those of a reduced-order numerical model based on the efficient DER formulation. We then explore the morphed shapes of different types of arrays, and find that some of these shapes are dependent on the snapping sequence – thus displaying "morphological" mechanical memory. However, memory is feeble in our structures, with some expected stable shapes not showing up in experiments due to specific parameter choices or fabrication imperfections. Finally, we explore the parametric space of the arrays and show that the existence of memory in these system depends on a careful selection of the geometrical design parameters. From a mechanics perspective, the most significant finding of our work is that, in our systems, stronger mechanical memory attributes do not necessarily stem from stronger coupling between units. Specifically, we unveil that different parameters affect memory differently depending on the shape of the arch and on the coupling between units: when coupling involves bending of the base between units, shorter distances between units are beneficial; when coupling involves twisting of the base between units, shorter distances between units can be detrimental. As a bottomline, the discrete nature of the coupling between arch and base in our structures can help unveil nuances about morphological mechanical memory that do not emerge from sheets featuring radially-symmetric dimples.

Future work could be aimed at providing more insight into the mechanics of these complex multistable structures. Specifically, it would be very valuable to reconstruct the energy landscape of our arrays from numerical simulations. Along the same lines, a much simpler alternative would be to investigate the force-deformation

response of arrays along specific, selected load paths. As the units in an array are snapped, changes in the base geometry are bound to influence the force-deformation response of the neighboring units. For example, when manually snapping units in our physical samples, we notice that some of the units take much higher force to snap if the nearest neighbors are snapped, compared to the case where no neighbor is snapped. Understanding these neighbor interactions could provide further insight on the fundamental ingredients needed for mechanical memory attributes to manifest.

Future work could focus on addressing current limitations related to manufacturing precision and computational predictive capabilities. To mitigate fabrication inconsistencies – which originate from the inherent non-uniformity of localized thermal processing – we could transition to fiber-reinforced composites. These materials offer the advantage of direct curing into the final, stress-free geometry, thereby eliminating the need for manual thermal post-processing. Furthermore, while the reduced-order DER model effectively captures the large-scale mechanics and kinematics of the units and the arrays, its accuracy diminishes when predicting the response of units involving substantial twisting. This deficiency can be resolved by extending the DER framework to explicitly model ribbon kinematics [60] by including axial-twisting coupling. Lastly, to accurately predict the bistability loss observed in specific polymeric samples, the model could benefit from the integration of viscoelasticity to account for time-dependent material behavior.

In this work, we focused on square-based units and their arrays – following our thought that the arrays would be simpler to analyze and provide a more fundamental understanding of their morphed configurations. A logical next step is to extend our investigation to other base shapes that allow for planar tiling, such as triangular or hexagonal, as shown in Fig. 13. We expect the morphed shapes of these new geometries to exhibit more

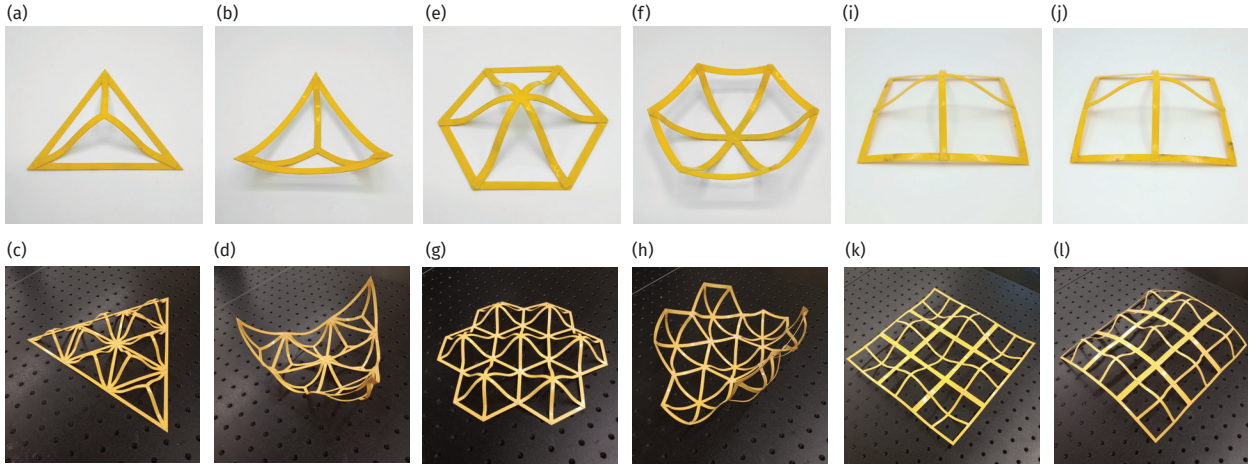


Fig. 13: Extensions of our idea. Future explorations could involve units with other footprints. (a,b) a triangular unit and (c,d) an array of the same unit, in their first and second stable states, respectively. (e,f) a hexagonal unit and (g,h) an array of the same unit, in their first and second stable states, respectively. A prestressed unit with square base, obtained by bonding flat base and arch precursors, (i) in its first and (j) second stable states, respectively. An array of those same units (k) in its original state, and (l) in a state in which all the downward units are snapped up.

intricate interactions than the square arrays, with the hexagonal unit potentially serving as a more direct analog to dimpled sheets. Future work could also involve arrays of prestressed units (similar to other works in the literature [75, 76]). The units presented in this paper are stress-free in their first stable state. Prestressed units can be prepared by directly bonding the flat, laser-cut parts without heat treatment. While fabrication of these units would be much simpler, the fact that their two stable states are almost identical in shape could limit the overall morphing capabilities of the arrays; it is also unclear how prestress would affect mechanical memory attributes.

Our work reports on the possibility of creating systems with mechanical memory attributes that are made of stiff materials. Thus, our structures could be integrated with mechanical computation devices based on vibrations and elastic waves, and act as memory storage units. Applying our structures in this realm would require detailed

studies of their dynamics, and on the possibility of snapping each unit with a vibration stimulus applied at the array's boundary. Moreover, pending studies on the load bearing capacity of the arrays, our dimpled frames could potentially find applications as morphing, lightweight architectural structures.


### Acknowledgments

P.C. and A.R. acknowledge support from the National Science Foundation (CMMI-2045191).


### Author Contributions

A.R.: Methodology; Software; Formal Analysis; Investigation; Resources; Visualization; Writing - Original Draft. P.C.: Conceptualization; Investigation; Writing - Review & Editing; Supervision; Funding Acquisition.

### Appendix A. Basics on Discrete Elastic Rods (DER)

In this section, we present a few basics on DER for the interested readers. The original DER formulation was proposed by Bergou et al. [48, 49], while the material presented here is mostly based on the book by Jawed et al. [77]. We also highlight the differences between our version of DER and their formulations.

A discrete elastic rod is a polygonal chain as shown in Fig.A.14a, which is intended to represent the centerline of a physical rod. The rod is discretized into $N$ nodes, defined by the position vectors $\mathbf{x}_0, \mathbf{x}_1, \cdots, \mathbf{x}_{N-1}$, which are connected by $N-1$ edges represented by the edge vectors $\mathbf{e}^0, \mathbf{e}^1, \cdots, \mathbf{e}^{N-2}$. In DER literature, subscripts are used for quantities associated with nodes, and superscripts for quantities associated with edges. As shown in Fig.A.14b, each edge $\mathbf{e}^k$ has two associated orthonormal frames: a material frame $\{\mathbf{m}_1^k, \mathbf{m}_2^k, \mathbf{t}^k\}$ and a reference frame $\{\mathbf{a}_1^k, \mathbf{a}_2^k, \mathbf{t}^k\}$. The two frames are separated by the rotational degree of freedom $\theta^k$, also known as twist angle, and they share the same unit tangent of the corresponding edge, defined by $\mathbf{t}^k = \mathbf{e}^k / \left\|\mathbf{e}^k\right\|$.

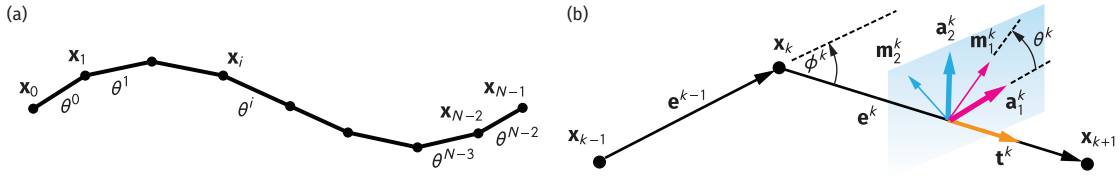


Fig. A.14: (a) A discrete elastic rod is represented by a polygonal chain, consisting of $N$ nodes having positional degrees of freedom $\mathbf{x}_0, \mathbf{x}_1, \cdots, \mathbf{x}_{N-1}$, and $N-1$ edges having rotational degrees of freedom $\theta^0, \theta^1, \cdots, \theta^{N-2}$. (b) Each edge vector $\mathbf{e}^k$ has two orthonormal frames: a material frame $\{\mathbf{m}_1^k, \mathbf{m}_2^k, \mathbf{t}^k\}$ and a reference frame $\{\mathbf{a}_1^k, \mathbf{a}_2^k, \mathbf{t}^k\}$, which are used to capture the rotation $\theta^k$ in that corresponding edge. The vector pairs $\{\mathbf{m}_1^k, \mathbf{m}_2^k\}$ and $\{\mathbf{a}_1^k, \mathbf{a}_2^k\}$ lie on the same plane which is normal to the tangent vector $\mathbf{t}^k$.

Each node has three positional degrees of freedom $(x_i, y_i, z_i)$ represented by the position vector $\mathbf{x}_i$ and each edge has one rotational degrees of freedom $\theta^k$, which sum up to $3N + (N-1)$ or $4N-1$ degrees of freedom for the rod expressed by the state vector

$$\mathbf{q} = \left[\mathbf{x}_0, \theta^0, \mathbf{x}_1, \theta^1, \cdots, \mathbf{x}_i, \theta^k, \cdots, \mathbf{x}_{N-2}, \theta^{N-2}, \mathbf{x}_{N-1}\right]^T. \tag{A.1}$$

The original DER formulation and the formulation presented in the book are position-based, which means that the state vector $\mathbf{q}$ is directly obtained by solving the equation of motion. However, in our formulation we solve for an equivalent displacement vector given by

$$\mathbf{u} = \left[\mathbf{u}_0, \Delta\theta^0, \mathbf{u}_1, \Delta\theta^1, \cdots, \mathbf{u}_i, \Delta\theta^k, \cdots, \mathbf{u}_{N-2}, \Delta\theta^{N-2}, \mathbf{u}_{N-1}\right]^T, \tag{A.2}$$

where $\mathbf{u}_0, \mathbf{u}_1, \cdots, \mathbf{u}_{N-1}$ are nodal displacements and $\Delta\theta^0, \Delta\theta^1, \cdots, \Delta\theta^{N-1}$ are torsional displacements of the edges. The state vector is then computed using $\mathbf{q}_t = \mathbf{q}_{t-1} + \mathbf{u}_t$, where $t$ represents current time step and $t-1$

is the previous time step. This modification of ours better aligns with the traditional finite element approach, where displacements are unknowns.

We now focus on discussing the strains and corresponding internal energies of a DER, which are divided into three categories: stretching, bending and twisting.

Among all the strains, the stretching strain of an edge $k$ is the easiest to compute and is given by

$$\varepsilon^k = \frac{\left\|\mathbf{e}^k\right\|}{\|\bar{\mathbf{e}}^k\|} - 1. \tag{A.3}$$

In DER literature, an "overbar" property, such as $\bar{\mathbf{e}}^k$ in this case, refer to the corresponding property in the undeformed (reference) configuration. Once the stretching strains are computed for all edges, the stretching energy is obtained by

$$E_s = \frac{1}{2}\sum_{k=0}^{N-2} EA^k(\varepsilon^k)^2 \left\|\bar{\mathbf{e}}^k\right\| \tag{A.4}$$

where $E$ is the material's Young modulus and $A^k$ is the undeformed cross sectional area of the edge.

The bending strains are computed by the vertex based curvatures $\kappa_{k_1}$ and $\kappa_{k_2}$ about the local axes 1 and 2 respectively in the cross sectional plane, given by

$$\kappa_{k_1} = \frac{1}{2}\left(\mathbf{m}_1^{k-1} + \mathbf{m}_1^k\right)\cdot(\kappa\mathbf{b})_k \quad \text{and} \quad \kappa_{k_2} = -\frac{1}{2}\left(\mathbf{m}_2^{k-1} + \mathbf{m}_2^k\right)\cdot(\kappa\mathbf{b})_k, \tag{A.5}$$

where $(\kappa\mathbf{b})_k$ is the discrete integrated curvature vector computed as

$$(\kappa\mathbf{b})_k = \frac{2\mathbf{t}^{k-1}\times\mathbf{t}^k}{1+\mathbf{t}^{k-1}\cdot\mathbf{t}^k}. \tag{A.6}$$

The norm of this vector is related to the turning angle $\phi_k$ shown in Fig.A.14b by the expression $\|(\kappa\mathbf{b})_k\| = 2\tan(\phi_k/2)$. The bending energy is then computed by adding energies for both local axes as

$$E_b = \frac{1}{2}\sum_{k=0}^{N-2}\frac{EI_{k1}}{\ell_k}(\kappa_{k1}-\bar{\kappa_{k1}})^2 + \frac{EI_{k2}}{\ell_k}(\kappa_{k2}-\bar{\kappa_{k2}})^2 \tag{A.7}$$

where $\bar{\kappa_{k1}}$ and $\bar{\kappa_{k2}}$ are the reference curvatures, $\ell_k$ is the Voronoi length define by $\ell_k = \left(\left\|\mathbf{e}^{k-1}\right\| + \left\|\mathbf{e}^k\right\|\right)/2$ , and $I_{k1}$, $I_{k2}$ are the second moments of area of the cross section.

The torsional strain is measured by the discrete integrated twist given by

$$m_{k+1} = \theta^{k+1} - \theta^k + \Delta m_{k+1}^{\text{ref}}, \tag{A.8}$$

where $\Delta m_{k+1}^{\text{ref}}$ is known as reference twist, a quantity that we refrain ourself to explain further and refer to the book as it involves exploring the concept of parallel transport and holonomy. The twisting energy is then computed by

$$E_t = \frac{1}{2}\sum_{k=0}^{N-2} GJ_k\frac{(m_k-\bar{m}_k)^2}{\bar{\ell_k}}, \tag{A.9}$$

where $G$ is the shear modulus of the material, $J_k$ is the polar moment of inertia, and $\bar{m}_k$ is the reference discrete integrated twist.

Once the individual energies are computed, the total energy is simply given by

$$E = E_s + E_t + E_b. \tag{A.10}$$

The internal forces (including moments) for each degree of freedom $u_i$ are expressed by

$$F_i^{\text{int}} = \frac{\partial}{\partial u_i}(E_s + E_t + E_b). \tag{A.11}$$

By using a simple forward-Euler time stepping algorithm, the dynamic equation of motion is given by

$$\mathbf{M}(\mathbf{u}_t - \mathbf{u}_{t-1})/\Delta t^2 - \mathbf{M}\mathbf{v}_{t-1}/\Delta t - \mathbf{F}^{\text{ext}}(t, \mathbf{u}_{t-1}, \mathbf{v}_{t-1}) - \mathbf{F}^{\text{int}}(\mathbf{u}_t, \mathbf{v}_t) = \mathbf{0}, \tag{A.12}$$

where $\mathbf{M}$ is the lumped mass matrix, $\mathbf{v}$ is the velocity vector, $\mathbf{F}^{\text{ext}}$ is the external force vector, and $\mathbf{F}^{\text{int}}$ is the internal force vector. The residual $\mathbf{R}$ is represented by the left-hand side of this equation. The damping forces are treated as an external forces on the nodes; for example, the damping force on node $k$ is computed as $\mathbf{F}^{\text{d}}_k = -\eta \ell_k \mathbf{v}_k$, where $\eta$ is a non-negative constant.

The Jacobian matrix $\mathbf{J}$ is obtained by taking derivatives of the residual with respect to the unknown $\mathbf{u}_t$, and in the forward-Euler case, it is computed as

$$\mathbf{J} = \mathbf{M}/\Delta t^2 + \mathbf{K}_T, \tag{A.13}$$

where $\mathbf{K}_T$ is the tangent stiffness matrix. Our preference for working with the tangent stiffness matrix, as opposed to using Hessians as in the original DER formulation, is what inspired us to use a displacement-based formulation instead of a position-based one in the first place. We use an incremental displacement technique, which allows to capture the negative stiffness region of the force displacement curve even with a Newton-Raphson algorithm. Finally, the displacement increment is computed as $\mathbf{du}_t = \mathbf{R}/\mathbf{K}_T$, which is used to update displacement vector via $\mathbf{u}_t = \mathbf{u}_{t-1} + \mathbf{du}_t$; once we achieve convergence, the last $\mathbf{u}_t$ is used to update the state vector $\mathbf{q}$.

## Appendix B. Torsional stiffness modifier

In this section, we discuss how we modified the torsional stiffness of the DER to better match with the torsional response of a strip of rectangular cross section (i.e., a ribbon). Let us assume the width and height of an edge $k$ in a DER to be $w^k$ and $h^k$ respectively, and define the vertex based width and height for each vertex as $w_i = (w^k + w^{k-1})/2$ and $h_i = (h^k + h^{k-1})/2$ respectively. From the DER literature, the torsional stiffness at a vertex is defined as $GJ_i$, where $G$ is the shear modulus of the material and $J_i$ is the polar moment of inertia defined as $J_i = A_i(w_i + h_i)^2/12$, where $A_i$ is the vertex-based area given by $A_i = w_i h_i$. However, this moment of inertia works best when $w_i$ and $h_i$ are comparable to each other, which is not the case for us, since we have $w = 5$ mm and $h = 0.5$ mm for each strip of the base. Therefore, to account for torsion-induced deformation in the ribbon-like cross section, we introduce a empirical constant $J$ and calibrate this property by comparing the 3D scan data for a single unit to our DER model.

Fig. B.15 shows the comparison between the 3D scan and model shape for different $J$ values. Fig. B.15a shows the second stable state of the plus unit we introduced earlier in the main text. We used the plus unit to calibrate the parameter $J$ since this is the unit where twist effects in the base are the largest. In Fig. B.15b-d, we present the deformed shape obtained when no modifier is used, i.e., if $J = 1.00$; Fig. B.15e-g show the comparison if $J = 0.50$; Fig. B.15h-j show the comparison for $J = 0.075$. We can see that, as $J$ gets smaller, the base shape of the modeled unit appears more and more square from the top view, which indicates a transition from bending-dominant to twisting-dominant deformation. For for $J = 0.075$, both the base shape and arch shape match well with the experiment; we use this same calibrated value $J = 0.075$ for all our simulations of single units and arrays.

## Appendix C. Damping in numerical simulations

Since all elements in our numerical models have a uniform short length, we simplify distributed viscous damping forces as acting on nodes; e.g., $\mathbf{F}^{\text{d}}_k$ is the force acting on node $k$. As introduced in Appendix Appendix A, the general damping force is $\mathbf{F}^{\text{d}}_k = -\eta \ell_k \mathbf{v}_k$. Due to the uniformity of $\ell_k$, this expression reduces to the effective nodal damping to

$$\mathbf{F}^{\text{d}}_k = -c\mathbf{v}_k, \quad \text{where } c = \eta \ell_k \tag{C.1}$$

where $c$ is the effective nodal damping coefficient.

The damping coefficients were determined empirically to ensure stable numerical convergence and to ensure that our simulations model a quasi-static process. For the models of the single units and the times array, no damping is required, resulting in $c = 0$. For the plus array we use $c = 5.0 \times 10^{-5}$ and for the and eight-leg array we use $c = 1.0 \times 10^{-4}$.

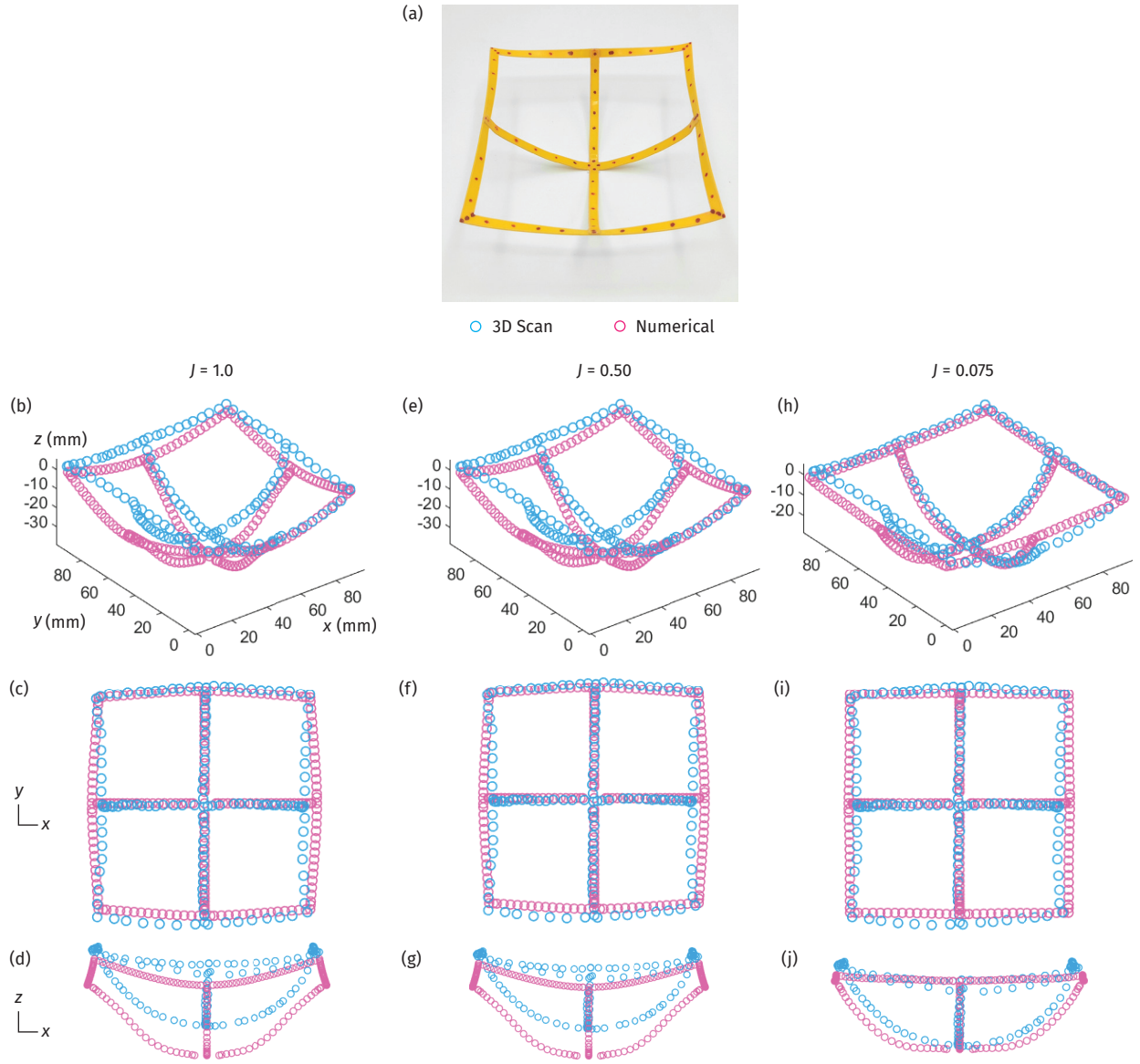


Fig. B.15: Torsional stiffness calibration by shape comparison of the plus unit. (a) The second stable state of the plus unit used for calibrating the torsional stiffness modifier, $J$, due to the maximum twist effect in its base. The 3D scan versus model prediction of the second stable state for the plus unit across three $J$ values are shown in the lower $3 \times 3$ panel, which shows the base transitioning from a curved shape to a straight line, indicating a shift from bending to twisting deformation and providing the best match for the base and arches, (b-d): deformed shape with no modifier, $J = 1.00$, (e-g): an intermediate modifier, $J = 0.075$. (h-j) the calibrated value $J = 0.50$. Using $J = 0.075$ also works best with the times and eight-leg unit.

## Appendix D. Experimental setup and fabrication details

A detailed sketch of the various components of our experimental setup for the testing of single units, with all its dimensions, is shown in Fig. D.16.

## Appendix E. Additional videos of experiments

To provide further information on the behavior of our physical samples, we report videos from the mechanical tests of one of the units, and videos of the sequential actuation of the units of some arrays. Each supplementary

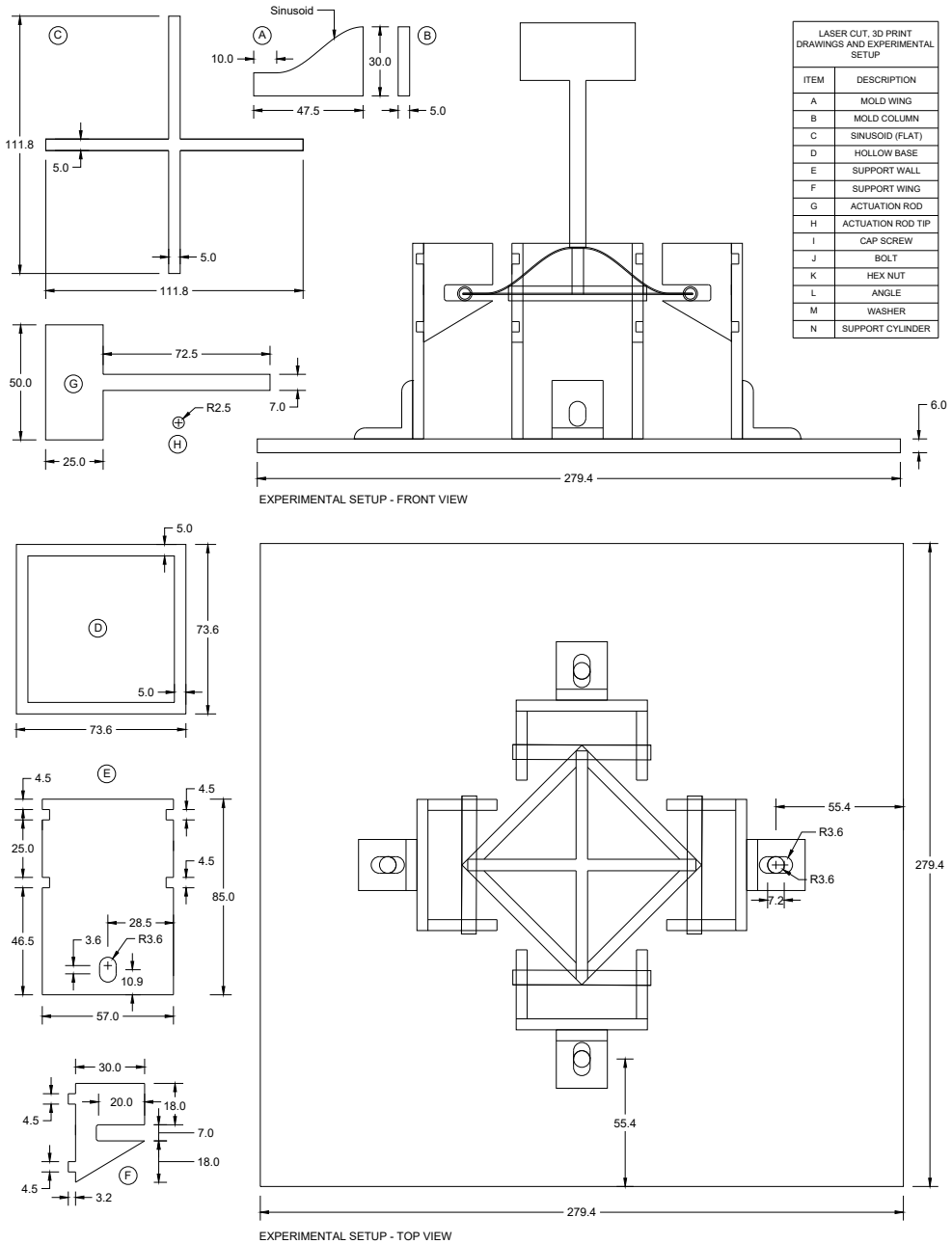


Fig. D.16: Details of laser cut, 3D printing and experimental setup. All dimensions are in millimeters.

video is described in the following.

- `PlusUnitMechanicalTest.mp4`: Mechanical test of the plus unit of height $h = 30$ mm, showing a secondary snapping at the 01m:26s timestamp, when the base strips suddenly straighten and the rollers moves apart from the center. This phenomenon is accompanied by a vertical jump in the force-deformation curve of Fig. 6h in the main text. A similar but opposite phenomenon in observed at timestamp 02m:38s, during unloading.

- `PlusArraySnapping.mp4`: In the single-width plus array, two neighbors cannot be snapped if they share the same edge. In this video, we try unsuccessfully to snap together the center unit and a neighboring one.

- `EightLegArraySwitchingDiagonal.mp4`: When all units are snapped, the double-width eight-leg array is multistable, and it can be switched between two diagonally-bent shapes by applying forces at the opposite corners. Both of these shapes are strong and the switching is smooth.

- `EightLegArraySwitchingOrthogonal.mp4`: The global morphed shape of a double-width, eight-leg array can be switched between two stable orthogonally-bent shapes, by applying forces at the opposite edges of the base. In this video, the center unit is not snapped here, as doing so causes only one of the two orthogonally-bent shapes to be stable (possibly due to fabrication errors).

## References


[1] S. Pellegrino, Deployable structures in engineering, in: Deployable structures, Springer, 2001, pp. 1–35.
[2] K. Bertoldi, V. Vitelli, J. Christensen, M. Van Hecke, Flexible mechanical metamaterials, Nature Reviews Materials 2 (11) (2017) 1–11.
[3] S. Barbarino, O. Bilgen, R. M. Ajaj, M. I. Friswell, D. J. Inman, A review of morphing aircraft, Journal of intelligent material systems and structures 22 (9) (2011) 823–877.
[4] T. A. Weisshaar, Morphing aircraft systems: historical perspectives and future challenges, Journal of aircraft 50 (2) (2013) 337–353.
[5] Y. Zhu, E. T. Filipov, Large-scale modular and uniformly thick origami-inspired adaptable and load-carrying structures, Nature Communications 15 (1) (2024) 2353.
[6] A. Tibert, S. Pellegrino, Review of form-finding methods for tensegrity structures, International Journal of Space Structures 18 (4) (2003) 209–223.
[7] A. Rafsanjani, Y. Zhang, B. Liu, S. M. Rubinstein, K. Bertoldi, Kirigami skins make a simple soft actuator crawl, Science Robotics 3 (15) (2018) eaar7555.
[8] E. W. Hawkes, L. H. Blumenschein, J. D. Greer, A. M. Okamura, A soft robot that navigates its environment through growth, Science Robotics 2 (8) (2017) eaan3028.
[9] G. M. Whitesides, Soft robotics, Angewandte Chemie International Edition 57 (16) (2018) 4258–4273.
[10] Y. Yang, K. Vella, D. P. Holmes, Grasping with kirigami shells, Science Robotics 6 (54) (2021) eabd6426.
[11] T. Kim, Y.-G. Lee, Shape transformable bifurcated stents, Scientific reports 8 (1) (2018) 13911.
[12] A. Kirillova, L. Ionov, Shape-changing polymers for biomedical applications, Journal of Materials Chemistry B 7 (10) (2019) 1597–1624.
[13] S. Shan, S. H. Kang, J. R. Raney, P. Wang, L. Fang, F. Candido, J. A. Lewis, K. Bertoldi, Multistable architected materials for trapping elastic strain energy, Advanced Materials 27 (29) (2015) 4296–4301. doi:10.1002/adma.201501708.
[14] T. R. Giri, R. Mailen, Controlled snapping sequence and energy absorption in multistable mechanical metamaterial cylinders, International Journal of Mechanical Sciences 204 (2021) 106541. doi:10.1016/j.ijmecsci.2021.106541.
[15] M. F. Daqaq, R. Masana, A. Erturk, D. Dane Quinn, On the role of nonlinearities in vibratory energy harvesting: a critical review and discussion, Applied mechanics reviews 66 (4) (2014) 040801.
[16] Y. Li, Y. Zhao, Y. Chi, Y. Hong, J. Yin, Shape-morphing materials and structures for energy-efficient building envelopes, Materials Today Energy 22 (2021) 100874.
[17] R. von Mises, Über die stabilitätsprobleme der elastizitätstheorie, ZAMM - Journal of Applied Mathematics and Mechanics / Zeitschrift für Angewandte Mathematik und Mechanik 3 (6) (1923) 406–422. doi:https://doi.org/10.1002/zamm.19230030602.
[18] M. Vangbo, An analytical analysis of a compressed bistable buckled beam, Sensors and Actuators A: Physical 69 (3) (1998) 212–216.
[19] D. P. Holmes, A. J. Crosby, Snapping surfaces, Advanced Materials 19 (21) (2007) 3589–3593.
[20] M. Santer, S. Pellegrino, Compliant multistable structural elements, International Journal of Solids and Structures 45 (24) (2008) 6190–6204.
[21] D. M. Kochmann, K. Bertoldi, Exploiting microstructural instabilities in solids and structures: from metamaterials to structural transitions, Applied mechanics reviews 69 (5) (2017) 050801.
[22] A. J. Lee, J. M. Fernandez, Inducing bistability in collapsible tubular mast booms with thin-ply composite shells, Composite Structures 225 (2019) 111166.
[23] T. Chen, J. Panetta, M. Schnaubelt, M. Pauly, Bistable auxetic surface structures, ACM Transactions on Graphics (TOG) 40 (4) (2021) 1–9. doi:10.1145/3450626.3459940.
[24] D. Melancon, B. Gorissen, C. J. García-Mora, C. Hoberman, K. Bertoldi, Multistable inflatable origami structures at the metre scale, Nature 592 (7855) (2021) 545–550.
[25] C. J. Garcia-Mora, J. Sanchez-Sanchez, Limitations in the design of deployable structures with straight scissors using identical elements, International Journal of Solids and Structures 230 (2021) 111171.

[26] I. Niloy, L. Annink, O. Silier, C. Daraio, P. Celli, Frustrated domes: From planar metamaterials to load-bearing structures, Extreme Mechanics Letters (2025) 102352.
[27] H. Yasuda, P. R. Buskohl, A. Gillman, T. D. Murphey, S. Stepney, R. A. Vaia, J. R. Raney, Mechanical computing, Nature 598 (7879) (2021) 39–48.
[28] A. Alù, A. F. Arrieta, E. Del Dottore, M. Dickey, S. Ferracin, R. Harne, H. Hauser, Q. He, J. B. Hopkins, L. P. Hyatt, et al., Roadmap on embodying mechano-intelligence and computing in functional materials and structures, Smart Materials and Structures 34 (6) (2025) 063501.
[29] C. Chen, P. Shi, Z. Liu, S. Duan, M. Si, C. Zhang, Y. Du, Y. Yan, T. J. White, R. Kramer-Bottiglio, et al., Advancing physical intelligence for autonomous soft robots, Science Robotics 10 (102) (2025) eads1292.
[30] T. Chen, M. Pauly, P. M. Reis, A reprogrammable mechanical metamaterial with stable memory, Nature 589 (7842) (2021) 386–390.
[31] T. Mei, Z. Meng, K. Zhao, C. Q. Chen, A mechanical metamaterial with reprogrammable logical functions, Nature communications 12 (1) (2021) 7234.
[32] J. R. Raney, N. Nadkarni, C. Daraio, D. M. Kochmann, J. A. Lewis, K. Bertoldi, Stable propagation of mechanical signals in soft media using stored elastic energy, Proceedings of the National Academy of Sciences 113 (35) (2016) 9722–9727.
[33] J. E. Pechac, M. J. Frazier, Mechanical multi-level memory from multi-stable metamaterial, Applied Physics Letters 122 (21) (2023).
[34] A. A. Watkins, G. Bordiga, M. Mu, V. Tournat, K. Bertoldi, Arbitrary mechanical memory encoding via nonlinear waves in bistable metamaterials, arXiv preprint arXiv:2508.20321 (2025).
[35] H. Yasuda, T. Tachi, M. Lee, J. Yang, Origami-based tunable truss structures for non-volatile mechanical memory operation, Nature communications 8 (1) (2017) 962.
[36] B. Treml, A. Gillman, P. Buskohl, R. Vaia, Origami mechanologic, Proceedings of the National Academy of Sciences 115 (27) (2018) 6916–6921.
[37] Z. Liu, H. Fang, J. Xu, K.-W. Wang, Cellular automata inspired multistable origami metamaterials for mechanical learning, Advanced Science 10 (34) (2023) 2305146.
[38] J. Byun, A. Pal, J. Ko, M. Sitti, Integrated mechanical computing for autonomous soft machines, Nature Communications 15 (1) (2024) 2933.
[39] K. Seffen, Mechanical memory metal: a novel material for developing morphing engineering structures, Scripta materialia 55 (4) (2006) 411–414. doi:10.1016/j.scriptamat.2006.03.028.
[40] J. A. Faber, J. P. Udani, K. S. Riley, A. R. Studart, A. F. Arrieta, Dome-patterned metamaterial sheets, Advanced Science 7 (22) (2020) 2001955. doi:10.1002/advs.202001955.
[41] J. P. Udani, A. F. Arrieta, Taming geometric frustration by leveraging structural elasticity, Materials & Design 221 (2022) 110809. doi:10.1016/j.matdes.2022.110809.
[42] M. Liu, L. Domino, I. D. de Dinechin, M. Taffetani, D. Vella, Snap-induced morphing: From a single bistable shell to the origin of shape bifurcation in interacting shells, Journal of the Mechanics and Physics of Solids 170 (2023) 105116. doi:10.1016/j.jmps.2022.105116.
[43] O. R. Bilal, A. Foehr, C. Daraio, Bistable metamaterial for switching and cascading elastic vibrations, Proceedings of the National Academy of Sciences 114 (18) (2017) 4603–4606.
[44] A. Darabi, E. Kliewer, M. J. Leamy, Reconfigurable acoustic multiplexer/demultiplexer using time division, Applied Physics Letters 119 (11) (2021).
[45] H. Pirie, S. Sadhuka, J. Wang, R. Andrei, J. E. Hoffman, Topological phononic logic, Physical Review Letters 128 (1) (2022) 015501.
[46] M. Mousa, M. Nouh, Parallel mechanical computing: Metamaterials that can multitask, Proceedings of the National Academy of Sciences 121 (52) (2024) e2407431121.
[47] A. Rahman, S. Ferracin, S. Tank, C. Zhang, P. Celli, Shape-retaining beam-like morphing structures via localized snap through, International Journal of Solids and Structures (2024) 112917.
[48] M. Bergou, M. Wardetzky, S. Robinson, B. Audoly, E. Grinspun, Discrete elastic rods, in: ACM SIGGRAPH 2008 papers, 2008, pp. 1–12. doi:10.1145/1399504.1360662.
[49] M. Bergou, B. Audoly, E. Vouga, M. Wardetzky, E. Grinspun, Discrete viscous threads, ACM Transactions on graphics (TOG) 29 (4) (2010) 1–10.
[50] D. M. Kaufman, R. Tamstorf, B. Smith, J.-M. Aubry, E. Grinspun, Adaptive nonlinearity for collisions in complex rod assemblies, ACM Transactions on Graphics (TOG) 33 (4) (2014) 1–12. doi:10.1145/2601097.2601100.
[51] L. Hu, D. Bradley, H. Li, T. Beeler, Simulation-ready hair capture, in: Computer Graphics Forum, Vol. 36, Wiley Online Library, 2017, pp. 281–294. doi:10.1111/cgf.13126.
[52] G. Daviet, Simple and scalable frictional contacts for thin nodal objects, ACM Transactions on Graphics (TOG) 39 (4) (2020) 61–1. doi:10.1145/3386569.3392439.
[53] M. Vidulis, Y. Ren, J. Panetta, E. Grinspun, M. Pauly, Computational exploration of multistable elastic knots, ACM Transactions on Graphics 42 (4) (2023) 1–15. doi:10.1145/3592399.
[54] M. K. Jawed, F. Da, J. Joo, E. Grinspun, P. M. Reis, Coiling of elastic rods on rigid substrates, Proceedings of the National Academy of Sciences 111 (41) (2014) 14663–14668. doi:10.1073/pnas.1409118111.
[55] M. K. Jawed, N. K. Khouri, F. Da, E. Grinspun, P. M. Reis, Propulsion and instability of a flexible helical rod rotating in a viscous fluid, Physical review letters 115 (16) (2015) 168101. doi:10.1103/PhysRevLett.115.168101.
[56] W. Huang, X. Huang, C. Majidi, M. K. Jawed, Dynamic simulation of articulated soft robots, Nature communications 11 (1) (2020) 2233. doi:10.1038/s41467-020-15651-9.
[57] V. Romero, M. Ly, A. H. Rasheed, R. Charrondière, A. Lazarus, S. Neukirch, F. Bertails-Descoubes, Physical validation of simulators in computer graphics: A new framework dedicated to slender elastic structures and frictional contact, ACM Transactions on Graphics (TOG) 40 (4) (2021) 1–19. doi:10.1145/3450626.3459931.
[58] W. Huang, C. Ma, L. Qin, Snap-through behaviors of a pre-deformed ribbon under midpoint loadings, International Journal of Solids

and Structures 232 (2021) 111184. doi:10.1016/j.ijsolstr.2021.111184.
[59] W. Huang, L. Qin, Q. Chen, Numerical exploration on snap buckling of a pre-stressed hemispherical gridshell, Journal of Applied Mechanics 89 (1) (2022) 011005. doi:10.1115/1.4052289.
[60] W. Huang, C. Ma, Q. Chen, L. Qin, A discrete differential geometry-based numerical framework for extensible ribbons, International Journal of Solids and Structures 248 (2022) 111619. doi:10.1016/j.ijsolstr.2022.111619.
[61] K. Korner, B. Audoly, K. Bhattacharya, Simple deformation measures for discrete elastic rods and ribbons, Proceedings of the Royal Society A 477 (2256) (2021) 20210561. doi:10.1098/rspa.2021.0561.
[62] C. Baek, A. O. Sageman-Furnas, M. K. Jawed, P. M. Reis, Form finding in elastic gridshells, Proceedings of the National Academy of Sciences 115 (1) (2018) 75–80. doi:10.1073/pnas.1713841115.
[63] J. Pérez, B. Thomaszewski, S. Coros, B. Bickel, J. A. Canabal, R. Sumner, M. A. Otaduy, Design and fabrication of flexible rod meshes, ACM Transactions on Graphics (TOG) 34 (4) (2015) 1–12. doi:10.1145/2766998.
[64] J. Panetta, M. Konaković-Luković, F. Isvoranu, E. Bouleau, M. Pauly, X-shells: A new class of deployable beam structures, ACM Transactions on Graphics (TOG) 38 (4) (2019) 1–15. doi:10.1145/3306346.3323040.
[65] C. Lestringant, D. M. Kochmann, Modeling of flexible beam networks and morphing structures by geometrically exact discrete beams, Journal of Applied Mechanics 87 (8) (2020) 081006. doi:10.1115/1.4046895.
[66] L. Qin, W. Huang, Y. Du, L. Zheng, M. K. Jawed, Genetic algorithm-based inverse design of elastic gridshells, Structural and Multidisciplinary Optimization 62 (2020) 2691–2707. doi:10.1007/s00158-020-02639-8.
[67] W. Huang, L. Qin, M. Khalid Jawed, Numerical method for direct solution to form-finding problem in convex gridshell, Journal of Applied Mechanics 88 (2) (2021) 021012. doi:10.1115/1.4048849.
[68] Y. Chandra, I. Stanciulescu, L. N. Virgin, T. G. Eason, S. M. Spottswood, A numerical investigation of snap-through in a shallow arch-like model, Journal of Sound and Vibration 332 (10) (2013) 2532–2548. doi:10.1016/j.jsv.2012.12.019.
[69] Y. Zhou, W. Chang, I. Stanciulescu, Non-linear stability and remote unconnected equilibria of shallow arches with asymmetric geometric imperfections, International Journal of Non-Linear Mechanics 77 (2015) 1–11. doi:10.1016/j.ijnonlinmec.2015.06.015.
[70] L. Virgin, R. Wiebe, S. Spottswood, T. Eason, Sensitivity in the structural behavior of shallow arches, International Journal of Non-Linear Mechanics 58 (2014) 212–221. doi:10.1016/j.ijnonlinmec.2013.10.003.
[71] B. S. Cox, R. M. Groh, D. Avitabile, A. Pirrera, Exploring the design space of nonlinear shallow arches with generalised path-following, Finite Elements in Analysis and Design 143 (2018) 1–10. doi:10.1016/j.finel.2018.01.004.
[72] Y.-L. Pi, M. A. Bradford, Multiple unstable equilibrium branches and non-linear dynamic buckling of shallow arches, International Journal of Non-Linear Mechanics 60 (2014) 33–45. doi:10.1016/j.ijnonlinmec.2013.12.005.
[73] B. Moghaddasie, I. Stanciulescu, Equilibria and stability boundaries of shallow arches under static loading in a thermal environment, International Journal of Non-Linear Mechanics 51 (2013) 132–144. doi:10.1016/j.ijnonlinmec.2013.01.001.
[74] P. Harvey Jr, L. Virgin, Coexisting equilibria and stability of a shallow arch: Unilateral displacement-control experiments and theory, International Journal of Solids and Structures 54 (2015) 1–11. doi:10.1016/j.ijsolstr.2014.11.016.
[75] G. Risso, M. Sakovsky, P. Ermanni, Instability-driven shape forming of fiber reinforced polymer frames, Composite Structures 268 (2021) 113946. doi:10.1016/j.compstruct.2021.113946.
[76] Z. Shen, X. Hu, Z. Tang, Y. Xiao, S. Wang, X. Cheng, Y. Zhang, Curvature programming of freestanding 3d mesostructures and flexible electronics based on bilayer ribbon networks, Journal of the Mechanics and Physics of Solids 191 (2024) 105766.
[77] M. K. Jawed, A. Novelia, O. M. O'Reilly, A primer on the kinematics of discrete elastic rods, 2018. doi:10.1007/978-3-319-76965-3.